



universität  
wien

# MASTERARBEIT / MASTER'S THESIS

Titel der Masterarbeit / Title of the Master's Thesis

„Histological methods for CD90 and luciferase detection  
and fluorescence tomography based biodistribution  
analysis“

verfasst von / submitted by

Julia Scholda, BSc

angestrebter akademischer Grad / in partial fulfilment of the requirements for the degree of  
Master of Science (MSc)

Wien, 2020 / Vienna, 2020

Studienkennzahl lt. Studienblatt /  
degree program code as it appears on  
the student record sheet:

UA 066 606

Studienrichtung lt. Studienblatt /  
degree program as it appears on  
the student record sheet:

Masterstudium Drug Discovery and Development

Betreut von / Supervisor:

Univ. Prof. Dipl. Ing. Dr. Manfred Ogris

Mitbetreut von / Co-Supervisor:

Dr. Haider Sami



## ***Acknowledgements***

At this point, I want to thank everyone who contributed in establishment of this thesis and supported me during this time. This included especially Univ. Prof. Dipl. Ing. Dr. Manfred Ogris, who offered me this position in such a short notice. Also, I would like to express my sincere thanks to Dr. Haider Sami and Mag. Fatih Alioglu, who always stood by my side with their professional knowledge and open ears for every problem. I am thankful that I got the possibility to work in such a nice team, who simplified and sweetened every day in the lab, and to make some new friends. I am glad to have learnt a lot during this semester, which contains both technical stuff and a lot about myself.

Further, I want to thank my friends who emotionally supported my during the whole study and for proof-reading this thesis. Last but not least, I want to thank my family for giving me the opportunity to study with their financial support.



## Table of contents

<b>1. Introduction</b>	<b>9</b>
1.1. Histology	9
1.1.1. Histological staining methods	9
1.1.2. Lymphatic system, B cells and B16F10 melanomas	12
1.1.3. Thy-1 also known as CD90	13
1.1.4. Transgenic reporter animals	15
1.2. Fluorescence imaging data analysis	17
1.2.1. Fluorescent proteins	18
1.2.2. Fluorescent dyes	18
1.2.3. Fluorescence imaging	21
1.2.4. Characteristics of siRNA and its application in nanoparticles	22
<b>2. Materials and Methods</b>	<b>24</b>
2.1. Materials	24
2.1.1. Histology	24
2.1.2. Fluorescence imaging data analysis	27
2.2. Methods	27
2.2.1. Histology	27
2.2.1.1. Organ embedding	27
2.2.1.2. Cut organs embedded in paraffin	28
2.2.1.3. Buffer preparation	28
2.2.1.4. IHC staining of CD90	29
2.2.1.5. IHC staining of firefly luciferase	32
2.2.1.6. Mice used for IHC	32
2.2.2. Fluorescence tomography data analysis	33
2.2.3. Calibration curve	34
2.2.3.1. Workflow and timeline of siRNA-AF750 experiment	34
2.2.3.2. Workflow and timeline of auropolyplex experiment	35
2.2.3.3. Workflow and timeline of quantum dot experiment	36

2.2.3.4. Workflow and timeline of quantoplex experiment .....	37
<b>3. Results .....</b>	<b>38</b>
3.1. Histology.....	38
3.1.1. Hematoxylin and eosin staining of murine tissue.....	38
3.1.2. Effective CD90 detection via immunohistochemistry.....	39
3.1.3. Firefly luciferase detection via immunohistochemistry.....	46
3.2. Fluorescence tomography data analysis.....	47
3.2.1. Influence of changing threshold values on FLIT measurements .....	47
3.2.2. Tracking biodistribution of naked siRNA-AF750 after systemic administration .....	48
3.2.3. Tracking biodistribution of siRNA-AF750 based auropolyplexes after systemic administration.....	52
3.2.4. Tracking quantum dot biodistribution after systemic administration .....	54
3.2.5. Tracking quantoplex biodistribution after systemic administration.....	57
<b>4. Discussion.....</b>	<b>61</b>
4.1. Histology.....	61
4.1.1. IHC detection of CD90.....	61
4.1.2. IHC detection of firefly luciferase .....	63
4.1.3. Hematoxylin and eosin staining .....	63
4.2. Fluorescence tomography data analysis.....	64
4.2.1. Influence of changing threshold values on FLIT measurements .....	64
4.2.2. Biodistribution of siRNA-AF750 and QD based nucleic acid formulations.....	64
4.3. Conclusion.....	66

## **Aim of the thesis**

The present thesis focused on two major parts, namely, to detect and visualize proteins of interest by histological methods in a tumor model in mice, and to determine and semi-quantitatively analyze the biodistribution of fluorescently labelled micro- and nanosized compounds by fluorescence tomography. In the first part, the major aim was to efficiently detect the cell surface protein Thy-1, also known as CD90, in an implanted tumor and specific organs of mice via immunohistochemistry and to optimize existing staining protocols. Similarly, protocols were optimized to detect the reporter protein firefly luciferase in a transgenic reporter mouse strain. Hematoxylin and eosin staining should be used to evaluate immunohistochemical data, but also this protocol had to be optimized in advance. For the second part of this thesis, which was analysis of fluorescence tomography data, the aim was to examine the biodistribution of naked siRNA-AF750, auropolyplexes, quantum dots and quantoplexes after they were administered *in vivo* and tracked via 3D fluorescence imaging tomography. Cuboid regions of interests had to be drawn for measurement and data had to be compared to the results of 2D organ images. Before performing the whole analysis, the influence of threshold values, which represent background signal, on quantitative measurements had to be determined.

## Abstract

Thy-1, also known as CD90, is a cell surface glycoprotein expressed in neurons, endothelial cells, thymocytes and many other cell types and plays a role in, among others, inhibition of neurite growth and melanoma cell migration. In mice, there are two alleles resulting in two subtypes, Thy-1.1 and Thy-1.2, whereas there is only one in humans. A transgenic mouse model was used for histological characterization in this thesis, where the reporter gene luciferase is expressed under the control of a Thy-1.2 promoter element. B16F10 melanoma cells with high metastatic potential and an aggressive growth pattern were implanted. Positive staining indicating CD90 expression was detected in tumors, brain and endothelial cells and lymphatic vessels in the skin. Furthermore, CD90 and the correlating expression of the transgene firefly luciferase under the control of the Thy-1.2-Luc expression cassette were detected in murine tissue of a breast cancer mouse model. As expected, this was not the case for implanted tumor cells. Since histological methods are limited in their resolution, 3D imaging offers a powerful alternative. By combining fluorescence molecular tomography and computed tomography, *in vivo* real-time tracking of fluorescence emitting probes was achieved. To detect signals via fluorescence imaging tomography, fluorescence dyes like AF750 or quantum dots must be added to the formulations. To track biodistribution of naked siRNA, aurotoplexes loaded with siRNA, cadmium telluride quantum dots or polyethyleneimine-based quantoplexes, 3D images of living mice were taken at two different time-points after injection. Signals of each organ were marked by cuboid regions of interest and measured for further evaluation. To summarize, Thy-1 was efficiently detected in an implanted tumor of a Thy-1.2-Luc transgenic mouse model. Firefly luciferase was also successfully detected under control of the Thy-1.2-Luc expression cassette in a breast cancer mouse model via immunohistochemistry. Furthermore, the biodistribution of siRNA and nanoparticles was efficiently tracked. SiRNA mainly accumulated in the kidneys and aurotoplexes were found in bladder and kidneys. Quantum dots showed a weak signal in the kidneys and quantoplex application resulted in signals in liver and lungs.

**Keywords:** Thy-1, B16F10, immunohistochemistry, FLIT, siRNA, nanoparticles

## Zusammenfassung

Thy-1, auch CD90 genannt, ist ein Zelloberflächenglykoprotein, das in Neuronen, Endothelzellen, Thymozyten und vielen weiteren Zelltypen exprimiert wird. Unter anderem spielt das Protein eine Rolle bei der Hemmung des Neuritenwachstums und bei der Migration von Melanomzellen. Bei Mäusen werden zwei Allele, die zu den zwei Subtypen Thy-1.1 und Thy-1.2 führen, unterschieden. Beim Menschen gibt es hingegen nur eines. Für die histologische Charakterisierung wurde in dieser Arbeit ein transgenes Mausmodell verwendet, in dem das Reportergen Luciferase unter der Kontrolle des Thy-1.2 Promotorelements exprimiert wird. In diese Mäuse wurden zusätzlich B16F10 Melanomzellen mit einem hohen Metastasierungspotenzial und einem aggressiven Wachstumsmuster implantiert. Eine positive immunohistochemische Färbung, welche ein Indikator für CD90 Expression ist, konnte in Tumoren, Hirn- und Endothelzellen, sowie in Lymphgefäßen in der Haut festgestellt werden. Weiters wurden CD90 und die damit korrelierende Expression des transgenen Reportergens Luciferase unter der Kontrolle der Thy-1.2-Luc Expressionskassette in murinem Gewebe eines Brustkrebs-Mausmodells nachgewiesen. Bei den implantierten Tumorzellen war diese Expression erwartungsgemäß nicht der Fall. Da die histologischen Methoden in ihrer Auflösung begrenzt sind, bietet die 3D-Bildgebung eine leistungsstarke Alternative. Durch die Kombination von Fluoreszenz-Molekulartomographie und Computertomographie kann eine Echtzeitverfolgung *in vivo* von fluoreszenzemittierenden Substanzen ermöglicht werden. Diese Substanzen sind zum Beispiel AF750 oder Quantenpunkte, welche zu Formulierungen mit Nukleinsäuren hinzugegeben werden. Um die Biodistribution von nackter siRNA, mit siRNA beladenen Auropolyplexen, Cadmiumtellurid-Quantenpunkten oder Quantoplexten auf Polyethylenimin-Basis zu verfolgen, wurden 3D-Bilder von lebenden Mäusen zu zwei verschiedenen Zeitpunkten nach der Injektion aufgenommen. Die Signale jedes Organs wurden durch quaderförmige Interessensregionen markiert und zur weiteren Auswertung gemessen. Zusammenfassend lässt sich sagen, dass Thy-1 erfolgreich in einem implantierten Tumor eines transgenen Thy-1.2-Luc Mausmodells nachgewiesen wurde. Auch Luciferase konnte in einem Mausmodell für Brustkrebs effizient nachgewiesen werden. Darüber hinaus konnte die Biodistribution von siRNA und Nanopartikeln verfolgt werden. SiRNA sammelte sich verstärkt in den Nieren und Auropolyplexe wurden in der Blase und den Nieren gefunden. Quantenpunkte zeigten ein schwaches Signal in den Nieren und die Applikation von Quantoplexes führte zu Signalen in der Leber und der Lunge.

**Schlagwörter:** Thy-1, B16F10, Immunohistochemie, FLIT, siRNA, Nanopartikel



## 1. Introduction

This thesis is separated into two projects, one focuses on histological methods and staining and the other project is about the tomographic analysis of fluorescence *in vivo* data. For both projects, introduction is structured into two different sections.

### 1.1. Histology

Histology is defined as the study of tissues in the body. The term “histo” comes from the Greek word for “tissue” or “web”. Generally, tissues are consisting of two interacting components: cells and extracellular matrix (ECM) [1]. The ECM is formed by two main classes of macromolecules: polysaccharide glycosaminoglycans and fibrous proteins. Its main function is to regulate cellular functions like adhesion, migration, proliferation and differentiation [2]. To make tissues visible under the light microscope, they must be prepared in an appropriate manner, since the natural structure and molecular composition within the body have to be maintained. Fixation is used to avoid tissue degradation and digestion by enzymes. A very common fixative is formaldehyde diluted in phosphate buffered saline (PBS). This fixative triggers amine ( $\text{NH}_2$ ) groups in proteins to form methylene groups, which stabilize tissues via crosslinking. These crosslinked tissue sections are mechanically stable structures. Following fixation, embedding and sectioning are the next steps for tissue preparation. To facilitate this, solid media like paraffin or plastic resins are used. Through degradation and clearing, water and solvents are removed and replaced by paraffin. The prepared solid tissue block may then be cut with a microtome and further stained for light microscopy, for example with hematoxylin and eosin (H&E) or by immunohistochemistry (IHC). Histology is commonly used in pathology for biopsies, where tissue samples are removed during surgery to find out whether tumor growth is malignant or not [1].

#### 1.1.1. Histological staining methods

Hematoxylin and eosin (H&E) staining is commonly used for recognizing various cell types and morphologic changes. Its major advantage is its compatibility with most fixatives [3]. Hematoxylin stains acidic structures like DNA, RNA and glycosaminoglycans with a dark blue color. Eosin, however, stains collagen and cytoplasmic compounds pink [1]. Therefore, in a typical tissue nuclei are stained blue, whereas the ECM and the cytoplasm is stained in various shades of pink. A disadvantage of this staining method is its incompatibility with immunofluorescence. Hematoxylin can also be used as counterstain in IHC [3].

The principle of IHC is based on antibody-antigen interactions. To perform IHC, labeled antibodies are used to identify and determine the localization and presence of specific proteins [1]. For this method two different types of antibodies exist: monoclonal and polyclonal antibodies. Monoclonal antibodies are derived from the immune response of a single B cell, whereas polyclonal antibodies are derived from that of multiple B cells. Monoclonal antibodies are able to specifically detect a particular epitope on an antigen. Polyclonal antibodies, however, are a heterogeneous mix of antibodies and can recognize different epitopes on one antigen. Therefore, polyclonal antibodies are more likely to cross-react with other antigens. Since polyclonal antibodies are less expensive in production and show a higher affinity and sensitivity, they are more commonly used for general research applications [4]. In IHC, two different detecting methods exist, a direct and an indirect one. In the direct method, the antibody against the protein of interest is tagged with a fluorescent or enzymatic (e.g. peroxidase, alkaline phosphatase) label and binds directly and specifically to the protein. In the indirect method, a primary antibody against the protein of interest is bound by a secondary, labeled antibody made in an other species. The secondary antibody is raised against the antibodies from the host species of the primary antibody (Figure 1) [1].

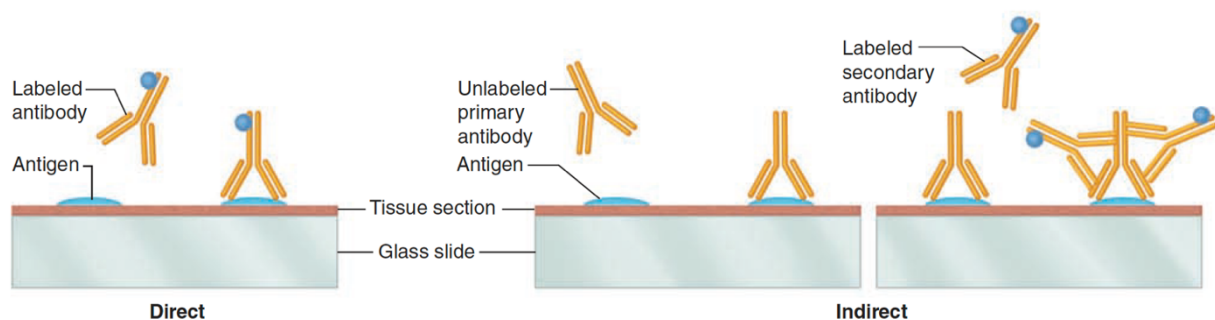


Figure 1: **Direct versus indirect detection method in immunohistochemistry.** In the direct detection method on the left, the labeled antibody against the protein of interest specifically binds to the antigen. In the indirect method on the right, the primary antibody is bound by a labeled secondary antibody (obtained from [1]).

The direct method is used to detect strongly expressed antigens. Advantages of this method are its fast application, because no additional blocking incubation step with a secondary antibody is needed, and the smaller probability of non-specific signal. The indirect method is often used for poorly expressed antigens because of signal amplification by the secondary antibody. Multiple secondary antibodies can bind to the same primary antibody. Additionally, the label and the detection method can be adapted more easily [5]. Since many cancer cells produce typical proteins, IHC can be used by pathologists to diagnose various diseases and tumor types [1].

Histologic samples can be detected by either fluorescent or chromogenic reactions. Fluorescent detection works via a fluorophore, which emits light when excited by a light source. The chromogenic method, on the other hand, takes advantage of chromogens undergoing a chemical reaction [6]. This method is used to obtain a more intense and sensitive signal than possible with fluorescence detection. The chromogenic detection method is based on enzymes bound to secondary antibodies which bind to primary antibodies against the protein of interest. A commonly used enzyme is horseradish peroxidase (HRP), which converts the chromogen 3,3'-diaminobenzidine (DAB) into a brownish precipitate after the addition of hydrogen peroxide through oxidation (Figure 2) [7]. The colored product is visible under the light microscope. DAB is a very photostable compound with long storage abilities. Also, DAB is insoluble in many solvents including alcohol, xylene and water, which makes it an ideal candidate for using standard histological techniques [8].

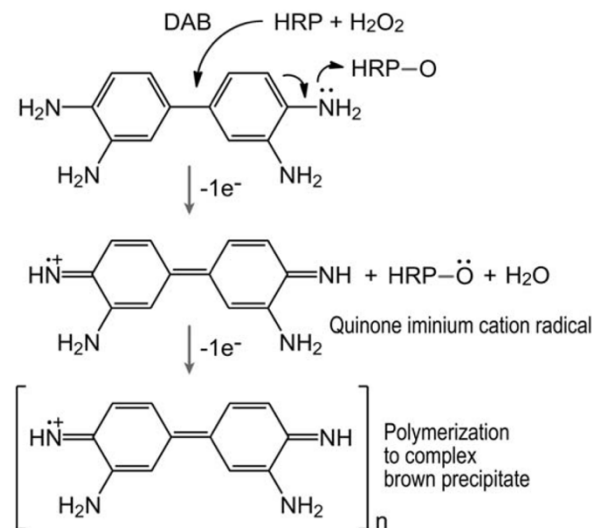


Figure 2: **Oxidation of DAB into brownish precipitate.** DAB donates an electron to HRP, which was catalyzed by the oxidation of hydrogen peroxide (obtained from [7]).

The chromogenic detection method can be divided into biotin based and non-biotin based methods. The biotin based method is performed with an avidin-biotin complex (ABC) or a labeled streptavidin-biotin binding (LSAB) complex. The non-biotin based method is done with a polymer complex or a micropolymer complex. The ABC (Figure 3), which is commonly used, is based on biotinylated secondary antibodies and an avidin-biotinylated peroxidase complex [9]. The protein avidin binds molecules of the vitamin biotin together. This results in a formation of a large complex, which is then attached to a biotinylated secondary antibody. Since there are always some biotin binding sites available on an ABC, more enzymes can be located at the antigen sites, resulting in increased sensitivity [10].

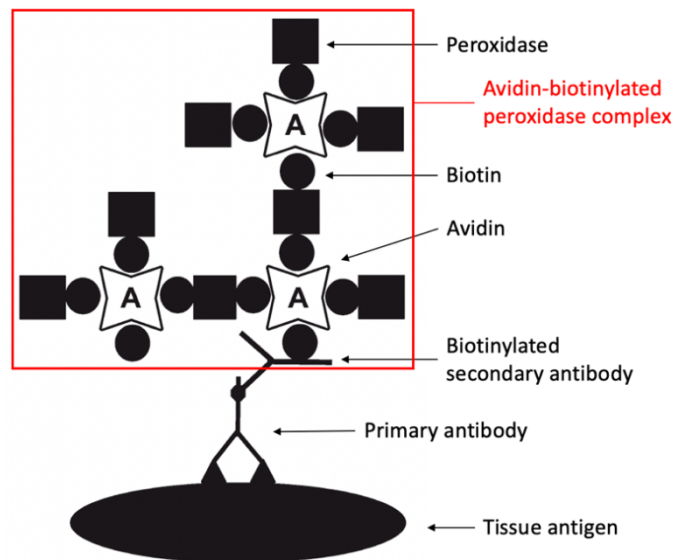


Figure 3: **Schematic diagram of the avidin-biotin complex (ABC) procedure.** Biotin forms a large complex together with avidin and peroxidase, which is attached to a biotinylated secondary antibody. The primary antibody raised against the antigen of interest is linked to the secondary antibody raised against the animal species the primary antibody was created in (adapted from [10]).

### 1.1.2. Lymphatic system, B cells and B16F10 melanomas

The circular fluids of the vertebrate body can be divided into two parallel vascular systems: the blood and the lymphatic vascular system [11]. The main function of the lymphatic system is to transport lymph, a fluid containing white blood cells, which are also called lymphocytes [12]. Furthermore, the lymphatic system plays a role in tumor metastasis and spread, chronic inflammatory disorders and transplant rejection [13]. Lymphocytes include B cells and T cells, which are essential to adaptive immunity, and natural killer cells, which are important for innate immunity. Tonsils, adenoids, the spleen and the thymus are the main part of the lymphatic system. B lymphocytes, also called B cells, stop infections spreading while producing specific antibodies to kill foreign microorganisms [12]. Other functions they have are antigen presentation, activation of T cells and regulatory properties, like regulation of tumor immunity [14]. As previous publications suggest, B cells can regulate tumor immunity in a positive and negative manner. For example, in B cell deficient mice, tumor immunity is regulated negatively in some murine tumor models, like B16F10 melanoma, EL4 thymoma and MC36 colon carcinoma [15]. In contrast, tumor growth is enhanced, when B cells are lacking anti-CD20 antibodies [16].

B16 is a murine melanoma model representing a transplantable tumor, which is syngeneic in the inbred mouse strain C57BL/6 and has been initially described by Fidler *et al.* in 1976 [17]. From humans it is known, that this melanoma is developing from melanocytes having a high metastatic potential in the lung and high resistance to chemotherapy. Although there are already approved some agents for cancer therapy by the Food and Drug Administration (FDA),

as for instance pegylated interferon alpha-2b, vemurafenib and ipilimumab, still further research is needed to find a drug with less severe side effects. Melanomas of the family B16 are for example B164A5, which is the most aggressive one, followed by B16F10, B16GMCSF and B16FLT3. All these types lead to increased levels of melanin and a brownish skin pigmentation within affected cells. This thesis mainly focuses on application of B16F10 in mice. F10 are bloodborne malignant melanoma cells comprising high metastatic potential in the lung. Also, these cells show an aggressive growth pattern shown by their ability to form colonies after local or intravenous injection. The number after the "F" (1-10) gives the number of cycles of lung colony formation. The higher the number (maximum 10), the higher the metastatic activity and the more aggressive the tumor. F1, however, exhibits only low metastatic activity [17] [18].

### **1.1.3. Thy-1 also known as CD90**

CD90 is a glycosylphosphatidylinositol (GPI)-anchored cell surface glycoprotein with a size of 25-37 kDa, encoded by a 5591-bp gene located in human chromosome 11q23.3 and in murine chromosome 9 [19] [20]. This protein is highly glycosylated and belongs to the immunoglobulin superfamily and to the lymphatic vascular system [13]. In mice, Thy-1 can be divided into two subtypes, Thy-1.1 and Thy-1.2, which differ only by one amino acid. In humans, however, only one allele of Thy-1 is present [19] [21]. Thy-1.1 comprises an arginine and Thy-1.2 a glutamine at position 89. Generally, Thy-1 consists of four exons. Exon 1, which occurs two times (1a and 1b), enables mRNA splicing in two variants and offers two transcription initiation sites. Exon 2 works as translation start site. Exon 3 encodes the amino acids 7 to 106 and exon 4 contains the C-terminal ending and the poly-A site. These last two exons together encode almost the whole Thy-1 protein sequence [20]. CD90 was firstly discovered in mice through the research for antisera against mouse leukemia cells in AKR mice by Reif in 1963 [22]. Subsequent research by the same scientist described CD90 as differentiation marker expressed mainly in the murine brain and thymus to differentiate between different mouse lymphocytes [13] [21]. However, nowadays it is known that it can be expressed in various murine and human tissues, for example in neurons, thymocytes, T cells, fibroblasts and endothelial cells, where CD90 is expressed exclusively at sites of inflammation or in tumors [11] [23]. Therefore, CD90 is involved in the regulation of for instance cell adhesion and migration, apoptosis, axon growth, T-cell activation and a lot more. Due to the fact that CD90 also plays an important role in cancer cell proliferation, metastasis and angiogenesis, it can be used as prognostic marker in many tumor types [19]. However, since Thy-1 is expressed to similar extends and has similar functions in mice and humans, it also plays an essential role in the human system.

Thy-1 signaling can be divided into cis and trans signaling. In cis-signaling, a protein binds to a membrane bound receptor, resulting in direct transmission of anti-inflammatory messages through the plasma membrane, although transmembrane domains are absent [24] [20]. This signaling works through interactions with Thy-1 crosslinking, T cell receptor (TCR), integral membrane proteins, kinases of the Src family or other still unknown mechanisms [25] [20]. Different mechanisms triggered by cis signaling are visualized in Figure 4B. When Thy-1 is expressed on neurons, thymocytes, mesangial cells or T cells, an inhibited neurite extension further leading to cell death is triggered. Thy-1 expression in fibroblasts results in altered phenotypic responses to adhesion proteins, cytokines and growth factors. Thy-1 expression on mesangial cells as well on T cells leads to a changed proliferation behavior. Furthermore, the expression on T cells can result in augmented TCR signaling. On carcinoma cells, Thy-1 expression leads to tumor suppression (Figure 4B) [25].

In trans signaling, a protein, in this case Thy-1, binds to integrins, which are transmembrane receptors, on the target cell. This triggers transmission of pro-inflammatory messages [24]. Suitable ligands for Thy-1 are  $\beta_2$  and  $\beta_3$  integrins. For example, Thy-1 on human dermal microvascular endothelial cells (HDMEC) binds to  $\alpha_X\beta_2$  or  $\alpha_M\beta_2$  on leukocytes, which results in promoted adhesion and trans-endothelial migration. When Thy-1 on HDMEC binds to melanoma cells via  $\alpha_V\beta_3$ , melanoma metastasis is enhanced. Binding to the same receptor in astrocytes leads to focal adhesion changes (Figure 4A) [25].

## Thy-1 (CD90) Signaling

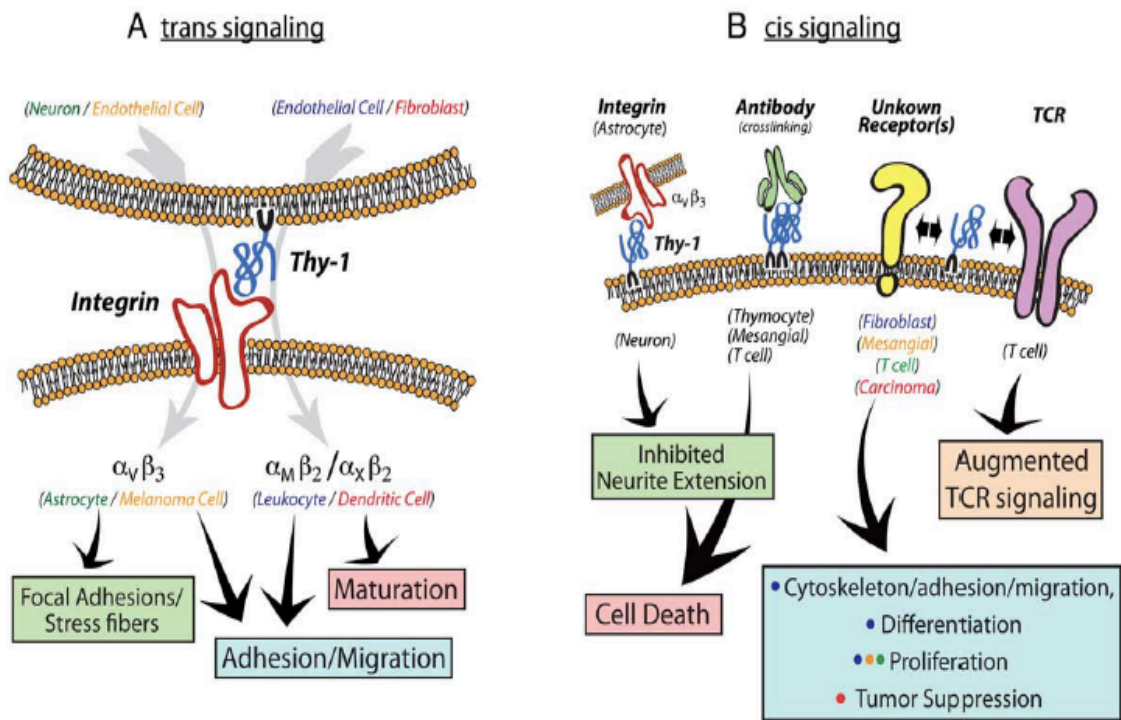


Figure 4: **Thy-1 (CD90) signaling.** **A.** Trans signaling. Thy-1 binds to integrins in target cells to trigger specific mechanisms (indicated by the arrows). **B.** Cis signaling. Signaling works through interactions with integrins, antibodies, TCR or still unknown receptors. The reactions triggered are indicated by the arrows (obtained from [25]).

### 1.1.4. Transgenic reporter animals

The introduction of transgenes can be used to study the functions and expression of certain genes in foreign species *in vivo*. Caroni (1996) found that the expression cassette derived from the murine Thy-1.2 gene can be used to realize a constitutive and strong transgene expression in neurons. Therefore, this cassette provides ideal conditions to express for instance the abundant proteins GAP-23 and GAP-43, which are usually expressed at very low levels in adult neurons. An advantage of using this cassette is that transgene expression starts the day after birth, therefore the interference with the early nervous system can be avoided. Also, the expression cassette is very sensitive because it offers a large variety of expression patterns which are integration-site dependent. Furthermore, the study by Caroni (1996) resulted in the conclusion that the expression is mostly restricted to neurons. Expression was also weakly detected in the lung, but this can be neglected. In neurons, the expression is established in the second week after birth and found to be constitutive in adults. With his study, Caroni (1996) established a modified Thy-1.2 expression cassette containing parts of the 3'-untranslated sequence including also the Thy-1 mRNA polyadenylation site (Figure 5). However, the cassette is designed in a way that all transgenes should include individual translation initiation sites [26].

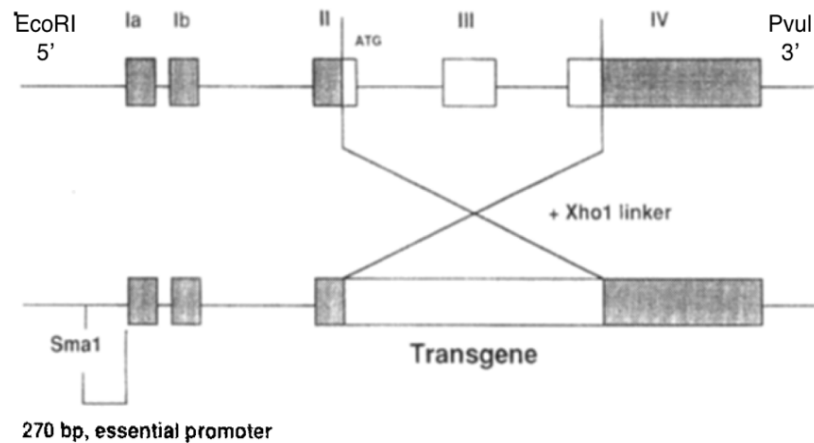


Figure 5: **Thy-1.2 expression cassette.** The cassette contains parts of a 3'-untranslated sequence and is flanked by an EcoRI (5' end) and a PvuI (3'site) (modified from [26]).

Reporter mice for the expression of fluorescent proteins like enhanced green fluorescent protein (EGFP) or yellow fluorescent protein (YFP) can be generated via introducing the Thy-1.2 expression cassette into the brain (Figure 5), which was initially developed by Caroni in 1996, as explained above [26]. The extensive expression of Thy-1 in the brain, especially neural cells, was initially described by Barclay *et al.* in 1976 and further reported in more detail by Feng *et al.* in 2000 [27] [28]. These fluorescent proteins are used to mark the activation of the Thy-1 promoter. For better signal to noise ratio and other advantages explained below, the application of luciferase or fluorescent proteins in the near infrared (NIR) would be desirable. In 2014, Josvay *et al.* generated a transgenic mouse strain expressing YFP under control of the Thy-1.2 expression cassette in neurons. In this experiment, Thy-1 promoter activity could be shown at tumor sites, sites of inflammation and during wound healing [23]. In contrast, the Thy-1.2-Luc transgenic mouse generated at the MMCT lab expresses luciferase. To localize this sensitive luciferase expression and to correlate it with CD90 protein localization, immunohistochemical stainings were performed, as also described in this thesis.

Reporter genes like luciferases can be used either in fluorescent or bioluminescent approaches. For emitting fluorescence, however, a light source capable of exciting the illuminated material is necessary, whereas bioluminescence works by using appropriate substrates [29]. Generally, luciferase is an oxidative enzyme emitting light in an ATP-dependent process. For example, luciferase homologues are firefly luciferases, which are commonly used for research, and fatty acyl-CoA synthetases. Firefly luciferase is derived from the North American firefly species *Photinus pyralis*. Its protein structure is shown in Figure 6A. In the presence of molecular oxygen, adenosine triphosphate (ATP) and magnesium, D-luciferin is oxidized by firefly luciferase to oxyluciferin (Figure 6B). This oxidation enables luciferin to produce light at a peak of 560 nm [30] [31]. In combination with bioluminescence imaging (BLI), the emitting light of

luciferase expressing cell lines can be used as detection system acting as a reporter to image for instance the function and localization of tumor cells *in vivo* [32] [29].

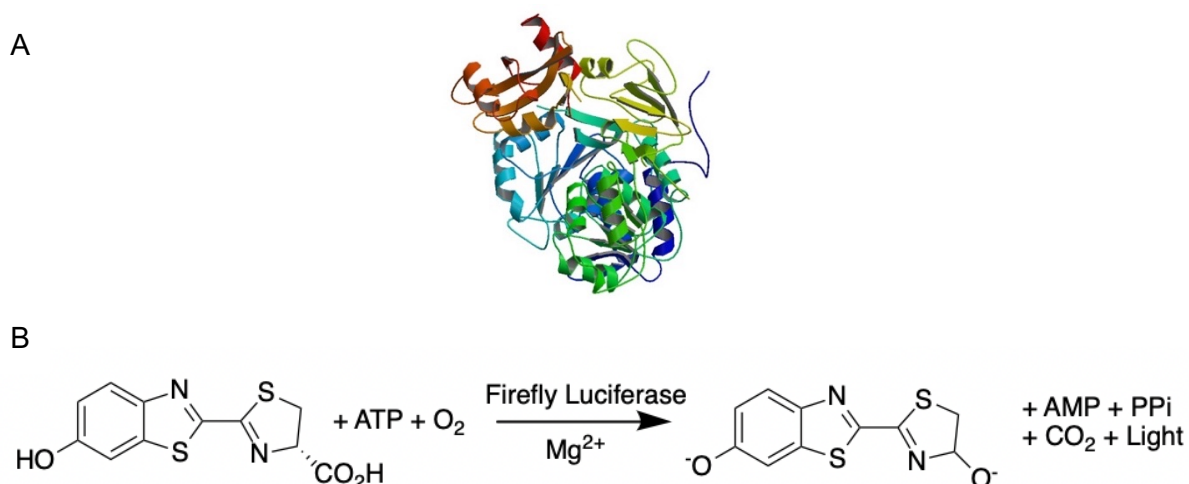


Figure 6: **Protein structure and oxidation of D-luciferin to oxyluciferin.** **A.** Protein structure of firefly luciferase (1LCI) [33]. **B.** D-luciferin is oxidized in presence of firefly luciferase, adenosine triphosphate, magnesium and oxygen to oxyluciferin emitting light at a peak of 560 nm [31].

Bioluminescence is a form of chemiluminescence and shows some advantages regarding the preclinical use over fluorescence. For example, bioluminescence is known to have a 10 to 1000-fold higher sensitivity than fluorescence because background signal can be excluded. In fluorescence imaging, however, the high photon influx can lead to high background signal [34]. In nature, this mechanism of mediated bioluminescence producing visible light is used to attract potential mating partners [29]. Therefore, another advantage of bioluminescence is its natural production, which is independent of an excitation light source. As long as the substrate is available, signal is visible. Additionally, since no excitation light is needed, no phototoxicity or photobleaching can occur, which is the reason for the statement that the use of bioluminescence is well suitable for live cell imaging [35]. Nonetheless, bioluminescence also has its disadvantages. For instance, the brightness of fluorescent proteins can easily be enhanced by increasing the amount of excitation light. Bioluminescence, however, is restricted by the amount of substrate molecules oxidized by luciferase in the reaction shown in Figure 6B. Therefore, it is necessary to increase exposure time, limiting temporal resolution [35].

## 1.2. Fluorescence imaging data analysis

Optical imaging is a powerful tool to perform *in vivo* tracking of biomolecules. Since optical imaging is a very sensitive method, it is possible to detect low concentrations of a target molecule. For detection, fluorescent dyes, bioluminescent or fluorescent proteins can be used [36].

### 1.2.1. Fluorescent proteins

Fluorescent proteins are naturally occurring chromophores. However, nowadays also engineered chromophores are available. In principle, fluorescent proteins are excited by a photon at a high energy level and emit a photon in form of light at a lower energy state. They have a broad light spectrum including light from far red to near infrared. One major advantage of fluorescent proteins is that they are genetically encoded, which means that the gene can be incorporated in cell lines triggering expression of these chromophores. But this advantage also implicates a disadvantage because fluorescent protein expression needs some time and cell modification has to be done in advance to the experiment. Further, fluorescent proteins are degraded proteolytically in the cell, which reduces their life span. Other disadvantages are their large size, low brightness and limited photostability [37]. An example for a fluorescent protein is the green fluorescent protein (GFP), which was first isolated in 1962 by Shimomura *et al.* from the jellyfish *Aequorea victoria* [38]. The cDNA of GFP encodes a polypeptide with 283 amino acids and a molecular weight of 27 kDa [39]. GFP emits bright green light at an emission peak of 509 nm when exposed to blue to ultraviolet light [40]. In 2008, Tsien was rewarded with the nobel prize in chemistry for successful discovery and modification of GFP [41]. Another example for fluorescent proteins is the red fluorescent protein (RFP), which was discovered in 1999 by Matz *et al.* and isolated from the coral *Discosoma* [42]. Its brightest mutant is called *Katushka* and has an emission peak at 635 nm, whereas less bright mutants are for instance *mCherry* or *mTomato* [39].

In contrast to fluorescent proteins, bioluminescent proteins convert chemical energy to light, as already explained in Figure 6 and its correlating sections. Bioluminescent proteins can be divided into photoproteins and luciferases. Photoproteins emit light in an amount dependent on the protein concentration. Luciferases emit light in proportion to the concentration of the substrate, which is luciferin [43]. The general principle and characteristics of luciferases are explained above.

### 1.2.2. Fluorescent dyes

Fluorescent dyes, which are also called fluorophores, cannot be genetically introduced into cells and are therefore commonly used in combination with labeled antibodies. In general, fluorophores absorb light at a high energy level and emit the absorbed light at a lower energy and longer wavelength. Advantages of fluorophores are their high brightness and photostability compared to fluorescence proteins. However, they have to be added each time before the experiment because brightness decreases significantly when exposed to light over a longer period of time [37]. Also, it is possible to generate tandem dyes, which comprise of two different and covalently attached fluorophores to enable multi-colored imaging. In this application, one

fluorophore acts as donor, which absorbs light, and the other fluorophore acts as acceptor, which emits light. The energy is transferred from the donor to the acceptor via fluorescence resonance energy transfer (FRET). For example, Alexa Fluor 488 and PE-Cy7 can be excited by a single blue laser, resulting in light emission of different colors, which have to be measured by color-specific detectors [44].

Since *in vivo* tomographic measurements can be ideally detected through signals in the far red and near infrared (NIR) spectrum, NIR dyes are an interesting field for research. The advantage over other staining methods, like fluorescence proteins, is that NIR dyes are not affected by hemoglobin absorption at lower wavelengths. When GFP would be used for this application, no fluorescence could be detected due to absorption. Also, NIR dyes offer a high signal to noise ratio due to less tissue absorption and autofluorescence. However, a disadvantage of NIR dyes is their high molecular weight, which is about 1 kDa, in comparison to radionuclides [45]. NIR ranges from approximately 630 to 800 nm and to date several Alexa fluor and cyanine dyes, which are comparable in their function and application, are developed. (Figure 7) [46]. Alexa fluor dyes are often chosen due to their high photostability over time. However, in contrast to cyanine dyes, this dye exhibits lower signal intensities and weaker levels of gene expression [47]. Examples for commonly used NIR dyes are AF750 and Cy7, which are spectrally similar. AF750 has its excitation peak at 752 nm, which is very close to that of Cy7 having the peak at 756 nm [46].

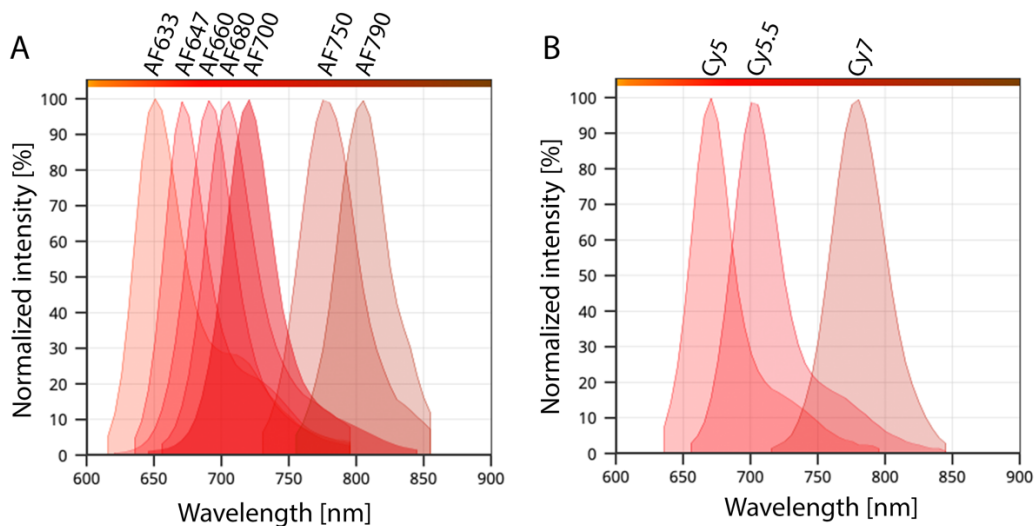


Figure 7: **Emission spectra of Alexa fluor and cyanine dyes in the near infrared.** **A.** Emission spectra of Alexa fluor dyes(633-790). **B.** Emission spectra of cyanine dyes (Cy5, Cy5.5, Cy7). The diagrams were created by aat-bio.com [46].

Another example for fluorophores are quantum dots. Quantum dots are small particles with 1-6 nm in diameter built of a semiconducting material. The most common materials quantum dots are produced of is cadmium in combination with selenide (CdSe) or telluride (CdTe) [48]. CdTe quantum dots, which were used for experiments in this thesis, are very small (< 5 nm) because no additional shells are needed. Due to their size, they are emitting light in the NIR spectrum, which can visualize obtained results *in vivo* [49]. Current researches suggest that the unique properties of quantum dots combine to offer monodispersity, luminescence and low toxicity. To date, no other nanocarriers comprising of these properties are developed. Although cadmium is cytotoxic, this generally causes no major problem for fluorescent dyes, unless they are not exposed to radiation or illumination. However, literature concerning cytotoxicity is inconclusive. On the one hand, no toxicity was reported, but on the other hand, cytotoxicity occurring due to surface ligands, Cd<sup>2+</sup> leakage or nanoparticle aggregation was observed by other researchers. Some major advantages quantum dots exhibit, compared to other fluorophores, are their gradually increasing levels of absorption directly correlating with increasing wavelength and their narrow emission band, which comprises a symmetrical shape. Also, quantum dots have an extraordinary high quantum yield with photon emission ranging from the UV up to the near infrared (NIR) wavelengths [48]. The spectrum of the emitted light can be changed by the size and composition of the quantum dots to green, yellow, orange or near infrared. All these mentioned benefits result in efficient and rapid elimination of quantum dots with a diameter smaller than 5.5 nm of the body [49]. Below this threshold, quantum dots were observed to be charged neutral, not interacting with serum proteins. Furthermore, they can be filtrated by the kidneys, which results in the essential advantage of reduced toxicity. However, quantum dots with a cationic or anionic surface shell interact rapidly with serum proteins leading to an increase in size (> 15 nm), which makes renal excretion impossible. The reason for this is the pore size of mammalian vasculature, which is usually lower than 5 nm. If the particles are smaller than this, equilibrium between these and the extracellular space can be reached fast. But if the nanoparticles tend to be bigger, transport across the endothelium occurs slower. Nanoparticles, which cannot be excreted renally, have to go through the liver leading to some problems. To overcome the first-pass mechanism and to prevent instant degradation, quantum dots have to be coated, which again increases size. Elimination into the bile is ineffective and requires more time. This long-term retention increases toxicity, however, this could be avoided through renal clearance [50]. Disadvantages, which are also reported by other fluorophores, are photochemical instability and non-ideal spectroscopic features. Even though quantum dots are a promising upcoming technique, especially the design of the surface shell has to be improved, since this component influences cytotoxicity, stability and fluorescence quantum yield highly [48]. An upcoming section will dive deeper into how quantum dots may be applied, specifically in quantoplexes.

### 1.2.3. Fluorescence imaging

One example for optical imaging is fluorescence imaging (FLI), allowing real-time tracking of NIR emitting probes *in vivo*. For this method, the excitation of a fluorophore and subsequent emission of light is required. The advantages of FLI in preclinical research are the research of biomarkers, biological processes and biodistribution of drug carriers and macromolecules. FLI can be combined with fluorescence molecular tomography for reconstructing fluorescence images. Since this technique exhibits bad spatial resolution in comparison to other imaging techniques like computed tomography (CT) or magnetic resonance imaging (MRI), it is commonly used in combination with other imaging modalities [51]. In combination with CT, the detailed localization of a signal in an organ can be determined. For CT, X-ray measurements are taken from different angles to calculate a 3D image representing a whole animal [52]. To analyze and evaluate this data, fluorescence imaging tomography (FLIT) and diffuse light imaging tomography (DLIT) are used. FLIT generates a 3D reconstruction for fluorescence light source distribution inside an object. DLIT does the same with luminescent light [53].

For FLIT measurement, also known as correlative FMT/CT measurement, the IVIS Spectrum CT Imaging device (by Perkin Elmer ® Inc.) can be used, as it was done in this thesis. FLIT is a transillumination fluorescent imaging method meaning that the light source is on the opposite side than the optical camera. An advantage of this method is the close proximity between the camera and the animal, enabling better tissue penetration. The light source has an extended NIR range and is adjustable, allowing a scan of the whole region of interest within the animal, which is anaesthetized and fixed on a grid plate. X-ray CT is used in this measurement to create a 3D tomography image. After imaging, the data can be reconstructed and evaluated with the corresponding Living Image ® software (version 4.5.2., Perkin Elmer). The general principle of FLIT measurement is described in Figure 8 [36].

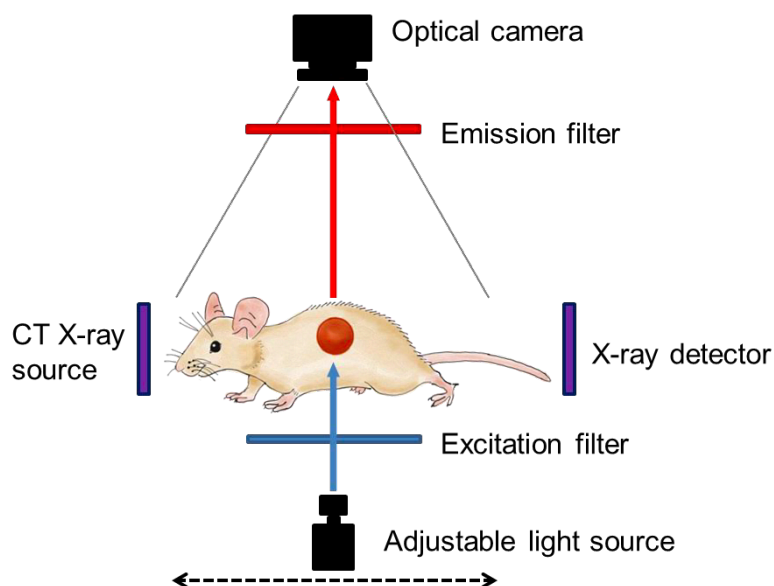


Figure 8: **Principle of fluorescence imaging tomography (FLIT)**. FLIT is a transillumination fluorescent imaging method because the adjustable light source is placed opposite the optical camera. This method is suitable for reconstructing 3D tomography images and deep tissue imaging (obtained from [36]).

#### 1.2.4. Characteristics of siRNA and its application in nanoparticles

Small interfering RNA (siRNA) is a useful tool to investigate gene functions via the knockdown of therapeutic targets at the transcriptional level with the aid of RNA interference (RNAi). Due to the high potential of this method, the establishment of efficient delivery methods is of major interest [54]. siRNA is administered locally to overcome interactions with blood components, the vascular system and the poor delivery rate. Due to its reduced systemic side-effects and high lung retention, pulmonary delivery methods, which include inhalation, intranasal and intratracheal administration, are commonly used. Besides finding the best route of administration, which is still of high interest for researchers, also various technological approaches are necessary for efficient delivery of nucleic acid applications. Towards this goal, nanoparticulate carriers play a major role [45]. Nanoparticles are particulate structures having a size of about 100 nm. They have a high surface to mass ratio, which enables them to absorb and carry other compounds like drugs and proteins. Nanoparticles are prepared from natural or synthetic polymers including materials like lipids or lactic acids. The goal of the establishment of nanoparticles is to find more specific targeting and delivery methods, the reduction of toxicity and higher biocompatibility [55]. To detect siRNA properly with CT, MRI or positron emission tomography (PET), siRNA can be labelled covalently with fluorescent dyes, for example with the NIR emitting dye Alexa Fluor 750 (AF750) for quantitative biodistribution analysis. Histology, however, is no suitable method for siRNA detection, since re-distribution events and dynamic changes cannot be observed. To increase the delivery rate to the target organ, siRNA can be incorporated into nanoparticles like auropolyplexes, quantum dots or quantoplexes [45].

By adding thiolated linear polyethylenimine (LPEI) to gold nanoparticles, cationic nanocarriers can be produced to increase siRNA formulation and delivery efficiency *in vitro* and *in vivo*. Further, siRNA and a LPEI polymer can be added to these cationic nanoparticles to generate auropolyplexes. The use of auropolyplexes enables efficient cellular uptake and exact control of loading efficiency, which results in an efficient gene knockdown. The lung is a popular target for drug delivery because of its high surface area and its close contact to the blood circulation. Because of this and their low toxicity, auropolyplexes are commonly administered intratracheally for successful drug delivery [56] [57].

To track bioactive compounds like siRNA in living animals, quantum dots or quantoplexes can also be used. Quantoplexes, however, are novel nanocarriers, which incorporate negative charged near-infrared (NIR)-emitting cadmium telluride (CdTe) quantum dots, polyethyleneimine (PEI) and a macromolecular drug like siRNA. All these components interact electrostatically and form virus-sized drug carriers. According to previous studies, quantoplexes rapidly accumulate in the lung, liver and spleen [58]. An advantage of quantoplexes is the possibility of screening early and rapid occurring biodistribution events *in vivo* and in real time. Also, a low concentration of the nanocarrier is enough to detect intense signal [59].

## 2. Materials and Methods

### 2.1. Materials

Table 1, Table 2, Table 3 and Table 4 list all reagents, machines, materials and software including their supplier used in the experiments described in this thesis.

#### 2.1.1. Histology

Table 1: List of used reagents including their supplier and catalog nr (alphabetical order sorted by reagents).

Reagent	Supplier	Location	Catalog Nr.
1-step anti-goat polymer-based IHC DAB kit	Vitro Vivo Biotech, LLC	Rockville (Maryland, USA)	VB-6026D
3,3'-diaminobenzidine tetrahydrochloride (DAB)	MP Biomedicals, LLC	Waltham (Massachusetts, USA)	08980681
35% hydrogen peroxide	Carl Roth GmbH + CoKG	Karlsruhe (Germany)	9683.1
96% ethanol	Carl Roth GmbH + CoKG	Karlsruhe (Germany)	T171.2
99.8% ethanol (denatured)	Carl Roth GmbH + CoKG	Karlsruhe (Germany)	K928.2
Ammonium hydroxide solution	Sigma-Aldrich (Merck KGaA)	Darmstadt (Germany)	221228
Bovine Serum Albumin (BSA)	Sigma-Aldrich (Merck KGaA)	Darmstadt (Germany)	A9647
Dulbecco's Phosphate buffered saline (PBS)	Sigma-Aldrich (Merck KGaA)	Darmstadt (Germany)	D8537
Entellan	Merck KGaA	Darmstadt (Germany)	107961
Eosin Y solution	Sigma-Aldrich (Merck KGaA)	Darmstadt (Germany)	318906
Ethylenediaminetetraacetic acid (EDTA)	Sigma-Aldrich (Merck KGaA)	Darmstadt (Germany)	E6758

Goat IgG isotype control	Abcam plc.	Cambridge (GB)	bs-0294P
Hematoxylin solution acc. to Harris	Carl Roth GmbH + CoKG	Karlsruhe (Germany)	X903.3
Hydrochloric acid	Sigma-Aldrich (Merck KGaA)	Darmstadt (Germany)	30721
Normal goat serum	Vector Laboratories, Inc.	Burlingame (California, USA)	S-1000-20
Paraformaldehyde	AppliChem GmbH	Darmstadt (Germany)	A3813
Paraplast	Sigma-Aldrich (Merck KGaA)	Darmstadt (Germany)	P3558
Primary goat antibody to firefly luciferase	Abcam plc.	Cambridge (GB)	ab181640
Primary rabbit antiCD90 polyclonal antibody	Abcam plc.	Cambridge (GB)	ab190940
Recombinant rabbit IgG, monoclonal [EPR25A] -	Abcam plc.	Cambridge (GB)	ab172730
Rabbit serum to INP	BIRD-C GmbH	Vienna (Austria)	2
Tri-sodium citrate dihyd- rate (Tris)	VWR International	Radnor (Pennsylvania, USA)	27.833.237
Triton X-100	Sigma-Aldrich (Merck KGaA)	Darmstadt (Germany)	X-100
Tween20	AppliChem GmbH	Darmstadt (Germany)	A4974
Vectastain ABC HRP Kit (Peroxidase, rabbit IgG)	Vector Laboratories, Inc.	Burlingame (California, USA)	PK-4001
Xylene	Carl Roth GmbH + CoKG	Karlsruhe (Germany)	9713.4

Table 2: **List of used machines including their supplier** (alphabetical order sorted by machine).

<b>Machine</b>	<b>Supplier</b>	<b>Location</b>
Light microscope BX53	Olympus K. K.	Tokio (Japan)
pH meter "InoLab 7710"	Xylem Analytics (WTW)	Weilheim (Germany)
Rotation microtome "CUT 5062"	SLEE medical GmbH	Mainz (Germany)
Silicone bath	Carl Roth GmbH + CoKG	Karlsruhe (Germany)
Table cooling plate "Para Cooler Model A"	Thomas-medical-system GmbH	Mitterhofen (Austria)
Tissue embedding carousel "SLEE MTP"	SLEE medical GmbH	Mainz (Germany)
Vacuum pump	Vacuubrand GmbH+CO KG	Wertheim (Germany)

Table 3: **List of used materials including their supplier** (alphabetical order sorted by material).

<b>Material</b>	<b>Supplier</b>	<b>Location</b>
15 mL tube	STARLAB International GmbH	Hamburg (Germany)
50 mL tube	STARLAB International GmbH	Hamburg (Germany)
Cover slips	Carl Roth GmbH + CoKG	Karlsruhe (Germany)
Hydrophobic PAP-pen	Cedarlane Laboratories	Burlington (Kanada)
Microscope slides "Super Frost Plus"	Thermo Fisher Scientific GmbH	Waltham (Massachusetts, USA)
SteriFlip® 45 µm filtration system (50 mL)	Merck KGaA	Darmstadt (Germany)

Tissue embedding cassette "Simport Scientific Histosette II"	Thermo Fisher Scientific GmbH	Waltham (Massachusetts, USA)
--	-------------------------------	------------------------------

## 2.1.2. Fluorescence imaging data analysis

Table 4: List of used software including their supplier (alphabetical order sorted by software name).

Software	Supplier	Location
Adobe Photoshop CC2019	Adobe Inc.	San José (California, USA)
Living Image 4.5.2 (64-bit)	Perkin Elmer Inc.	Waltham (Massachusetts, USA)
Microsoft Excel version 16.35	Microsoft Corporation	Redmond (Washington, USA)

## 2.2. Methods

In the following paragraphs the methods and necessary preparations of each experiment are described in detail for ideal reproducibility. The methods are listed in chronologic order, in which the experiments were performed.

### 2.2.1. Histology

Histological methods, which are explained in detail below, are organ embedding, cutting organs embedded in paraffin, buffer preparation and immunohistochemical staining. IHC staining methods of CD90 and firefly luciferase will be described in the next paragraphs.

#### 2.2.1.1. Organ embedding

After intratracheal instillation fixation, the organs were stored in 70% ethanol. Intratracheal instillation fixation was done to maintain all organ and cell structures. This was done via direct administration of the fixation agent, which was in this case paraformaldehyde, through a catheter into the lung without injuring any organs [60]. First, a list containing all information about the organs had to be established. Next, alcohol was discarded and the organs were prepared for formalin penetration. Organs which were too big for embedding were sliced to ensure penetration. Following this step, the organs were put into a fresh 15 mL tube and filled up with 10% formalin (4% formaldehyde in HBS). This was stored under the hood for 22 h in a horizontal

position. Afterwards, the formalin was discarded and the organs were placed in pre-labeled tissue embedding cassettes "Simport Scientific Histosette II" (Fisher Scientific GmbH, Waltham, Massachusetts, USA). During processing, the cassettes were stored in a beaker filled with 70% ethanol to prevent drying out. After checking, if all solutions were filled to cover the slices, the cassettes were put in the first bucket (70% ethanol) of the tissue embedding carousel "SLEE MTP" (SLEE medical GmbH, Mainz, Germany). The instructions on the display were followed and program 2, which is a specific program enabling delayed start of the machine by setting a timer and having a total duration of approximately 13 h, was started. The embedding station had to be warmed up approximately 45 min before embedding. To start with, the paraffin bowl, the surface and the cassette bowls were heated up to 60°C. Metal cassettes were put into the left bowl and the embedding cassettes including the organs were put into the bowl on the right side. Also, the filling level of Paraplast (Sigma-Aldrich (Merck KGaA), Darmstadt, Germany) had to be checked. Next, the cooling spot on the station and the cooling plate "Para Cooler Model A" (Thomas-medical-system GmbH, Mitterhofen, Austria) were turned on. For organ embedding, some drops of paraffin were poured into a metal cassette and the organ was placed into it. Then, the organ was pushed down softly while the paraffin cooled down on the cooling spot. The lid of the embedding cassette was then placed the sample, which was then filled with hot paraffin and then completely cooled down on the cooling plate.

### **2.2.1.2. Cut organs embedded in paraffin**

Ideally, all organs determined to be stained with H&E or immunohistochemistry had to be cut in the same week as staining would be performed. Firstly, the organs embedded in paraffin were cooled down for some minutes to reach the ideal cutting temperature, which was approximately -25°C. This was done with the table cooling plate "Para Cooler Model A" (Thomas-medical-system GmbH, Mitterhofen, Austria). Then, the organs were cut with a rotation microtome "CUT 5062" (SLEE medical GmbH, Mainz, Germany) at 2 µm. Subsequently, the sections were put on the surface of distilled water, which made it easier to place them onto the microscope slides "Super Frost Plus" (Thermo Fisher Scientific GmbH, Waltham, Massachusetts, USA), where they could dry overnight. Two replicates of each organ were placed on each slide. One slide for primary antibody and isotype staining and one for the buffer controls were prepared.

### **2.2.1.3. Buffer preparation**

To prepare the 10 mM sodium citrate buffer, ultrapure water (produced by machine by Sartorius AG, Göttingen, Germany) was mixed with tri-sodium citrate dihydrate (VWR International, Radnor, Pennsylvania, USA). After the reagents were dissolved in the solution facilitated by a magnetic stirrer, the pH was adjusted with 1 M HCl to pH 6. The pH was measured with the

pH meter “InoLab 7710” (Xylem Analytics, Weilheim, Germany). After this was done, 0.5 mL Tween20 (AppliChem GmbH, Darmstadt, Germany) were added to the mixture, which was then stored at 4°C.

To prepare Tris-EDTA buffer (+ 0.05% Tween20), 1 M EDTA (0.37 g) and ultrapure water (1000 mL, produced by machine by Sartorius AG, Göttingen, Germany) were mixed with Trisodium citrate dihydrate (1.21 g, VWR International, Radnor, Pennsylvania, USA). The pH was adjusted with NaOH to pH 9 and additionally 0.05% Tween20 (0.5 mL, AppliChem GmbH, Darmstadt, Germany) was added. The mixture was then stored at 4°C.

To prepare 2% BSA/PBS, 50 mL falcons were filled with each 1 g BSA (Sigma-Aldrich (Merck KGaA), Darmstadt, Germany) and 50 mL PBS (Sigma-Aldrich (Merck KGaA), Darmstadt, Germany). When BSA was dissolved after inverting, the mixture was filtered with a SteriFlip® 45 µL filtration system (Merck KGaA, Darmstadt, Germany), which was connected to a vacuum pump (Vacuubrand GmbH+CO, Wertheim, Germany).

#### **2.2.1.4. IHC staining of CD90**

For anti-CD90 staining, the sections were firstly heated in an oven at approximately 50°C for at least 2 h. When paraffin was melted and droplets began to form, the sections were further processed. In the meantime, everything necessary for heat induced epitope retrieval (HIER) was prepared. This included a heated pot filled with oil and a citrate buffer at pH 6. Also, the graded ethanol series and xylene of the deparaffinization, hydration and dehydration row were filled up, if necessary. For staining, a humidified chamber was prepared while putting wet tissues soaked in distilled water into it. After heating in the oven, the samples were put in the deparaffinization and hydration row. The deparaffinization step in xylene (Carl Roth GmbH + CoKG, Karlsruhe, Germany) was necessary to completely remove paraffin from the sections to provide better staining with less background [61]. After incubating three times for 5 min in xylene, the samples were directly put into 99.8% ethanol (Carl Roth GmbH + CoKG, Karlsruhe, Germany), an anhydrous alcohol, for 30 s. To prevent transfer of the clearant into lower alcohol concentrations, three stages for each ethanol concentration of the graded series were recommended. Also, an appropriate immersion time was necessary to ensure complete removal of the previous solutions. Following to incubation in 99.8% ethanol, the sections were incubated in 96% and 70% ethanol for each 30 s. Hydrating is generally necessary, since further IHC staining steps include anhydrous media like water or PBS. At the end of the hydration row, the samples were incubated once for 30 s in distilled water to rinse off all ethanol [61]. Following to this, the slides were put into a jar filled with HIER buffer, in this case citrate buffer at pH 6, which was put into the pre-heated oil bath at 121°C for 30 min. Here it should be considered

that the buffer needed additional 10 min to boil. HIER is performed to improve staining by modifying the molecular conformation of the epitopes, which are the target proteins. The result of unfolding cross-linked proteins with this method is enhanced antibody reactivity [62]. After boiling, the jar was put out of the oil bath and allowed to cool down for a few minutes under the hood. Then the lid was removed and the buffer was cooled down for 30 min to room temperature in the open. In the meantime, the blocking serum was prepared while mixing one drop of normal goat serum (Vectastain ABC HRP Kit (Peroxidase, rabbit IgG), Vector Laboratories, Inc., Burlingame, California, USA) with 3333  $\mu$ L 2% BSA/PBS (Sigma-Aldrich (Merck KGaA), Darmstadt, Germany) in a 15 mL tube (STARLAB International GmbH, Hamburg, Germany). After cooling down, the sections were washed three times with PBS washing buffer. It was ensured that the slides were always covered with PBS to prevent drying out. Drying out would cause high background staining because of non-specific antibody staining [61]. Then, the slides were washed with PBS, dried and circles were drawn with a hydrophobic PAP-pen (Cedarlane Laboratories, Burlington, Kanada) around the tissue sections to save reagents and antibodies. PAP stands for peroxidase-anti peroxidase, which is an older staining method used for signal amplification [63]. The next step was adding the blocking serum (Vectastain ABC HRP Kit (Peroxidase, rabbit IgG), Vector Laboratories, Inc., Burlingame, California, USA) to each section. The blocking serum, which is typically from an other species than the species in which the primary antibody was raised, blocks binding of Fc receptors to antibodies to reduce unspecific binding [61]. After 30 min incubation, the samples were washed with PBS and incubated for 15 min with 2 to 3 drops of avidin solution (Vectastain ABC HRP Kit (Peroxidase, rabbit IgG), Vector Laboratories, Inc., Burlingame, California, USA). Then the sections were washed again and incubated the same way with biotin (Vectastain ABC HRP Kit (Peroxidase, rabbit IgG), Vector Laboratories, Inc., Burlingame, California, USA). Avidin and biotin were part of the ABC blocking kit, which blocked endogenous biotin, biotin receptors and remaining avidin binding sites. This step was done to enhance results for low signal strengths and could have been omitted [64]. During incubation times, the primary rabbit anti-CD90 antibody (1:600, ab190940, Abcam plc., Cambridge, GB) and the rabbit igG isotype control (1:600, ab172730, Abcam plc., Cambridge, GB) were prepared. It was necessary to centrifuge the antibodies before use and to vortex after mixing. Also, they had to be diluted appropriately. In the following steps, the sections were washed with PBS and the primary antibody or isotype was added. The samples were incubated over night at 4°C.

The following day, 0.3% hydrogen peroxide in PBS was prepared. For this, 2.143 mL 35% H<sub>2</sub>O<sub>2</sub> (Carl Roth GmbH + CoKG, Karlsruhe, Germany) were mixed with 247.857 mL PBS. The primary antibody was drained from the sections and all samples were washed three times with

PBS washing buffer. Then, the slides were incubated in 0.3% H<sub>2</sub>O<sub>2</sub> for 15 min. Hydrogen peroxide was used to block endogenous peroxidase to prevent non-specific background staining caused by HRP conjugated antibodies. Since certain tissues or proteins, as for example the cell surface marker CD4, could be destroyed by hydrogen peroxidase, it had to be diluted to low concentrations [65]. In the meantime, the secondary antibody (Vectastain ABC HRP Kit (Peroxidase, rabbit IgG), Vector Laboratories, Inc., Burlingame, California, USA) was prepared. Also, the ABC reagent (Vectastain ABC HRP Kit (Peroxidase, rabbit IgG), Vector Laboratories, Inc., Burlingame, California, USA) was prepared via mixing 5 mL 2% BSA/PBS with one drop reagent A (Avidin ABC). After vortexing this properly, one drop of reagent B (Biotinylated HRP, ABC) was added and vortexed again. The readily mixed ABC reagent had to be mixed approximately 30 min before use. After incubation, the sections were washed with PBS and then incubated for 30 min with the secondary antibody. During incubation time, the DAB solution was prepared. For this, one tab DAB (MP Biomedicals, LLC, Waltham, Massachusetts, USA) was diluted in 10 mL distilled water on the magnetic stirrer. Since DAB is sensitive to light, the tube was covered with aluminum foil. After incubation, the slides were washed again with PBS and incubated with the ABC reagent for 30 min. This reagent was used to better detect and visualize biotinylated molecules due to resulting signal amplification. In the meantime, an additional jar filled with distilled water was prepared and hematoxylin was filtered. After incubation, the slides were washed again with PBS. In addition, each section was incubated with approximately 200 µL DAB solution for 2 min. The protein of interest was targeted with an antibody conjugated with a peroxidase enzyme (HRP). In presence with hydrogen peroxidase, DAB is oxidized and a chromogenic reaction turned the epitope sites into a brownish color. Therefore, DAB is commonly used in IHC to stain nucleic acids and proteins. [61]. The staining was checked under the light microscope (Olympus K. K., Tokyo, Japan) and if not intense enough, the sections were incubated again for a few seconds covered with DAB solution. The reaction was then stopped with the previously prepared jar filled with distilled water. To counterstain the nuclei, hematoxylin solution according to Harris (Carl Roth GmbH + CoKG, Karlsruhe, Germany) was used. To realize this, samples were incubated for 3 min in filtered hematoxylin, for 10 s in rinsing tap water, for 1 s in HCl-EtOH (Sigma-Aldrich/ Merck KGaA, Darmstadt, Germany), for 20 s in rinsing tap water, for 20 s in NH<sub>4</sub>-water (Sigma-Aldrich/ Merck KGaA, Darmstadt, Germany) and for 1 min in rinsing tap water. Additionally, the sections were put into the dehydration row. The gradually increased alcohol concentrations were used to remove water from tissue sections. The sections were incubated each three times for 1 s in 99.8%, 96% and 70% ethanol. The purpose of the subsequent clearing process with xylene was to remove all remaining hydrous compounds from the sections to enable coversliping them in an anhydrous medium [66]. In the first xylene jar, the samples were incubated for 1 min, in the subsequent two they were incubated for two minutes each. As last step, the

sections were mounted in Entellan (Merck KGaA, Darmstadt, Germany), an anhydrous mounting medium containing xylene, with cover slips (Carl Roth GmbH + CoKG, Karlsruhe, Germany).

### **2.2.1.5. IHC staining of firefly luciferase**

The first steps of anti-luciferase staining are identical to those performed for anti-CD90 staining. After heating in the oven, deparaffinization and hydration, all samples were transferred to Tris-EDTA buffer with 0.05% Tween20 (AppliChem GmbH, Darmstadt, Germany) and boiled at 121°C for 30 min. After antigen retrieval and cooling down to room temperature, all slides were incubated for 2 min in PBS/Triton X-100 (0.025%, Sigma-Aldrich/ Merck KGaA, Darmstadt, Germany) for better permeabilization of the cell wall. To prepare this, 62.5 µL Triton X-100 were mixed with 249.93 mL PBS over the magnetic stirrer. After incubation in PBS/Triton X-100, the samples were washed for 2 min in PBS washing buffer. Then, all slides were incubated with 1-2 drops of normal horse serum, which is part of the 1-step anti-goat polymer-based IHC DAB kit (Vitro Vivo Biotech, LLC., Rockville, Maryland, USA), for 30 min to block non-specific binding of immunoglobulin. After incubation and washing steps, the samples were incubated with either primary goat antibody to firefly luciferase (1:1000, ab181640, Abcam plc., Cambridge, GB), goat IgG isotype control (1:1000, bs-0294P, Abcam plc., Cambridge, GB) or PBS buffer over night at 4°C.

After incubation with 0.3% H<sub>2</sub>O<sub>2</sub> on the following day, all slides were incubated with 2-3 drops of the secondary antibody, which is part of the 1-step anti-goat polymer-based IHC DAB kit (Vitro Vivo Biotech, LLC., Rockville, Maryland, USA), or PBS buffer for 30 min at room temperature. The following washing steps, DAB incubation, counterstaining, dehydration and mounting were performed as already explained in the protocol of anti-CD90 staining.

### **2.2.1.6. Mice used for IHC**

For histochemical staining of CD90 and luciferase, tissue from transgenic mice expressing luciferase under control of the Thy-1.2 expression cassette according to Caroni were used [26]. These mice were established in the MMCT lab with C57BL/6-albino background. C57BL/6-albino mice (B6(C)/Rj-Tyrc/c, also termed B6 albino mouse (obtained from Janvier Labs (Le Genest-Saint-Isle, France))) lack pigmentation in skin due to an albino mutation and are better suited for BLI. Tissue from non-transgenic C57BL/6-albino mice was taken as control wildtype. In a separate set of experiments, lung tissue from a BALB/c mouse, which carried 4T1-luc tumors (from luciferase marked 4T1 triple negative murine breast cancer cells, initially explained by Geyer et al [67]), was stained. As a control, a similar mouse, but with 4T1 tumors

genetically marked with the fluorescent protein iRFP720 was utilized. Table 5 gives an overview of the mice used with their corresponding primary antibody types and strains.

Table 5: **Information to all mice used in IHC.** The information includes, whether the individual mouse is transgenic or wildtype. Also, information about the strain and primary antibody is added.

	<b>Mouse nr.</b>	<b>Strain</b>	<b>Primary antibody</b>
<b>Thy-1.2-Luc transgenic</b>	MCT-172	C57BL/6-albino	rabbit anti-CD90
	MCT-173		
	MCT-179		
<b>Wildtype</b>	MCT-356	C57BL/6	rabbit anti-CD90
	MCT-357		
	MCT-358		
<b>Wildtype</b>	M-113	BALB/c with 4T1-iRFP720 tumors	goat anti firefly luciferase
	M-106	BALB/c with 4T1-Luc tumors	

## 2.2.2. Fluorescence tomography data analysis

For 3D analysis, the software Living Image 5.4.2 (64-bit) (Perkin Elmer Inc., Waltham, Massachusetts, USA) was used. To begin with, one had to be logged in with a username and password. Following to this, a file could be opened and subsequently loaded. The mice could be depicted in either the supine (dorsal) or prone (ventral) position. However, for representation the supine position is more commonly used due to better visibility. When the image was loaded, firstly a mouse surface topography reconstructed from CT data was shown. Subsequently, the image had to be reconstructed for FLIT analysis by clicking on the reconstruct button in the section "FLIT 3D Reconstruction" of the tool palette. Then, the threshold had to be adjusted to reduce the background signal. It had to be considered that threshold values should be the same for every time in one project. A cuboid region of interest (ROI) was generated by clicking on the button showing a square in the "ROI Tools" section of the tool palette. Before the ROI could be changed, it had to be selected in the "3D ROI Transformation Tool". At this moment, it was possible to move the ROI, change its size and to rotate it by directly clicking on it. To change between these operations, TAB had to be pressed. Every ROI was set manually for each organ to cover the whole signal area. It had to be considered that each ROI should comprise approximately the same volume for every time in one project. This also considered the color, which can be changed by double clicking on the ROI. The final ROI size can be checked with the "Slice plane" option showing all axes (coronal, sagittal and transaxial) on the left side

of the screen. However, whole analysis is generally conducted in the maximum intensity projection (MIP) on the right side of the screen. The whole analysis should be saved and ideally screenshots for documentation. The last step of analysis was measuring all ROIs via clicking on “Measure 3D ROIs” in the “ROI Tools” section of the tool palette. For this, the section “3D ROI Measurement” was chosen and the data type was changed to “Source Voxels”. The measurement unit was determined as “total pmol”. This measurement was then exported as Excel file (.csv). In the following, the measurements were evaluated with Microsoft Excel version 16.35 (Microsoft Corporation, Redmond, Washington, USA) and the images saved as TIFF were prepared for visualization with Adobe Photoshop CC 2019 (Adobe Inc., Redmond, Washington, USA). Generally, the principle of data analysis was the same for every experiment and mouse. It was important that every step was done strictly according to the protocol to make data reproducible.

### 2.2.3. Calibration curve

With a calibration curve (Figure 9), the exact amount of AF750 in pmol to be applied to every mouse used for the siRNA-AF750 and auropolyplex experiments had to be calculated in advance. With the aid of this curve, FLIT analysis was quantified. The calibration curve was established according to the supplemental information of Geyer *et al.* (2017) [45].

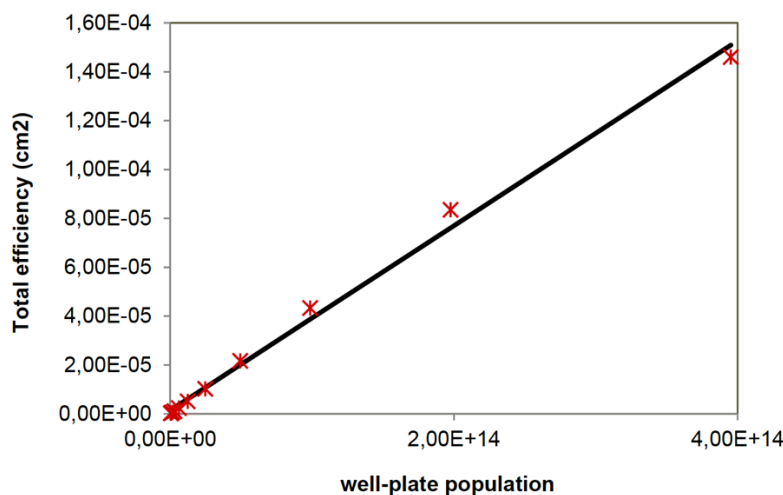


Figure 9: **Calibration curve for calculation of AF750 amount.** With this, the exact amount of AF750 to be applied into every mouse for the siRNA-AF750 and auropolyplex experiments was calculated.

#### 2.2.3.1. Workflow and timeline of siRNA-AF750 experiment

Three mice (MCT-361, MCT-362, MCT-363) of the strain B6 Albino CR were injected intravenously into the tail vein with 20  $\mu$ g siRNA-AF750. Based on the calibration curve shown in Figure 9, 1274 pmol AF750 was injected into every mouse. For this experiment two mice (MCT-

MCT-364, MCT-365) were taken as control. Naked siRNA were prepared in HEPES buffered glucose (HBG, 5 % glucose w/v, 20 mM HEPES pH 7.4) and injected at a dosage of 2.5 mg/Kg. Out of the total siRNA dosage per mouse, 20µg was AF750 labeled negative control siRNA and the rest was unlabeled negative control SSOs. Each of the treated mice was injected with the above dosage as per their body weight (MCT-361 – 183 µL, MCT-362 – 140 µL, MCT-363 – 147 µL). 1 h after injection of siRNA-AF750, they were injected intraperitoneally with 300 µL iopamidol. After waiting half an hour, 2D FLI and 3D FLIT images were taken in prone and supine position. Exactly 24 h after injection, mice were injected for a second time with iopamidol. After 0.5 h, 2D FLI, 3D FLIT, organ collection and organ imaging were performed. This experiment was done in 2019 by Karla Singeorzan and Mag. Fatih Alioglu. The exact workflow is visualized in Figure 10.

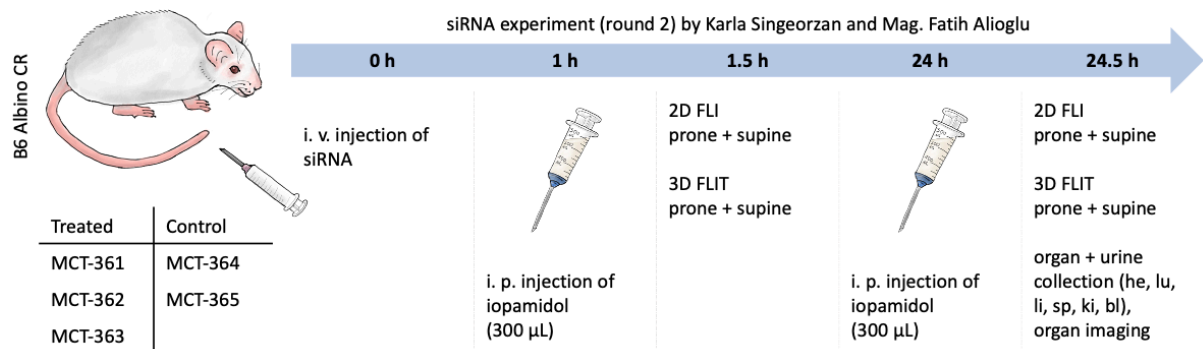


Figure 10: **Workflow and timeline of siRNA-AF750 experiment.** MCT-361, MCT-362 and MCT-363 were injected intravenously with siRNA-AF750. For contrast, mice were injected with iopamidol 30 min before imaging. 1.5 h and 24.5 h after initial injection mice were imaged via 2D FLI and 3D FLIT in prone and supine position. At the end of the experiment, organs were collected and imaged.

### 2.2.3.2. Workflow and timeline of auropolyplex experiment

Three mice (AGE-269, MCT-012, MCT-015) of the strain BALB/c were injected intratracheally with 10 µg siRNA-AF750 incorporated in auropolyplexes and intraperitoneally with 300 µL iopamidol. Based on that and the calibration curve shown in Figure 9, every mouse got injected with 637 pmol AF750. For this experiment no control mice were used. 30 min after injection, 3D FLIT imaging in prone and supine position was performed. 24 h after initial injection, mice were again injected with iopamidol. Half an hour later, 3D FLIT imaging was performed. This experiment was done in 2018 by Wolfram Polzer. The exact workflow is visualized in Figure 11.

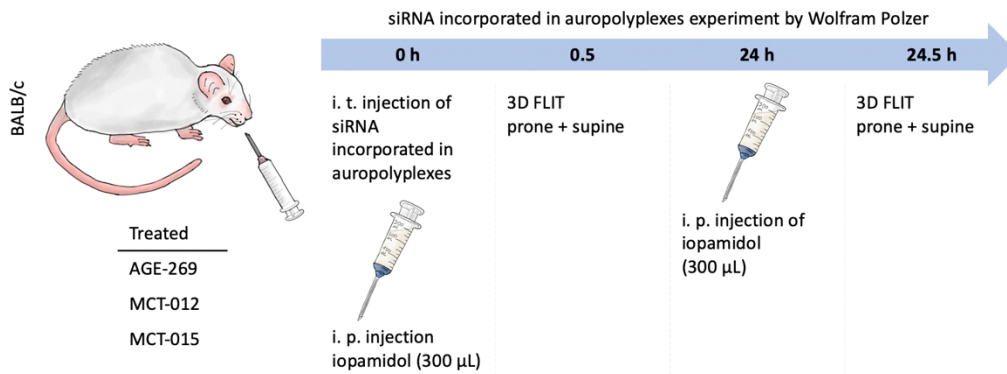


Figure 11: **Workflow and timeline of auropolyplex experiment.** AGE-269, MCT-012 and MCT-015 were injected intratracheally with siRNA-AF750 incorporated in auropolyplexes. For contrast, mice were injected with iopamidol 30 min before imaging. 0.5 h and 24.5 h after initial injection, 3D FLIT imaging in prone and supine position was performed.

### 2.2.3.3. Workflow and timeline of quantum dot experiment

Three mice (MCT-038, PRI-242, PRI-250) of the strain BALB/c were injected intravenously into the tail vein with CdTe quantum dots having a size of 4 nm. The quantum were injected at a dose of 6.9 mg cadmium per kg per mouse. Before injection of iopamidol, 2D FL spectral unmixing was done in prone and supine position. 30 min after injection of the contrast agent, 3D FLIT was performed. Exactly 24 h after initial quantum dot injection, a second round of 2D FL spectral unmixing was done. Half an hour later, mice were injected with iopamidol for a second time and analyzed by 3D FLIT, 2D FL spectral unmixing and *in situ* organ imaging. This experiment was done in 2017 by Manuela Simlinger and Prof. Manfred Ogris. The exact workflow is visualized in Figure 12.

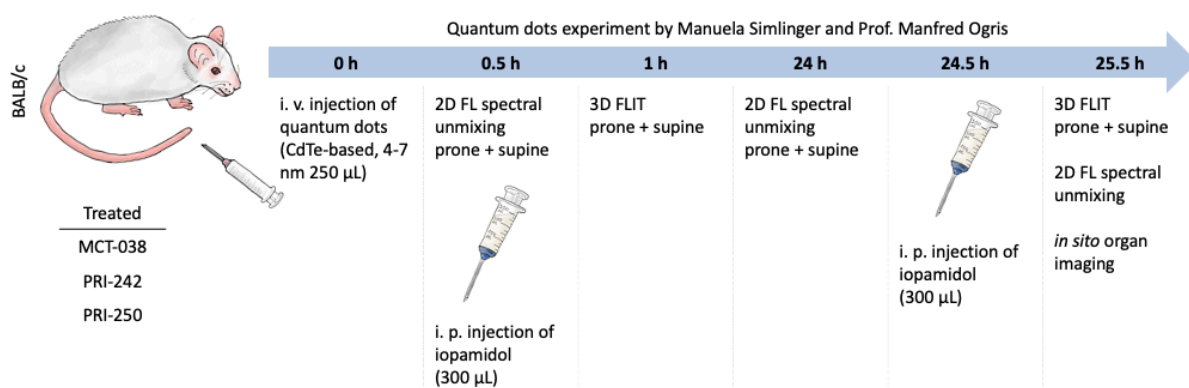


Figure 12: **Workflow and timeline of quantum dot experiment.** MCT-038, PRI-242 and PRI-250 were injected intravenously with CdTe quantum dots. For contrast, mice were injected with iopamidol 30 min before imaging. 1 h and 25.5 after initial injection mice were imaged with 3D FLIT in prone and supine position, 2D FL spectral unmixing and *in situ* organ imaging.

### 2.2.3.4. Workflow and timeline of quantoplex experiment

Four mice (MCT-031, MCT-036, MCT-037, MCT-040) of the strain BALB/c were injected intravenously into the tail vein with quantoplexes having a size of 180-220 nm. These quantoplexes were produced in-house and were incorporated with NIR-emitting quantum dots containing 17.26 µg of cadmium, polyethylenimine (PEI) and a macromolecular model drug, in this case siRNA. One mouse (MCT-038) was used as control. 30 min after quantoplex injection, mice were injected intraperitoneally with 300 µL iopamidol. After waiting half an hour, 2D FLI and 3D FLIT in prone and supine position was performed. 24 h after initial quantoplex injection, mice were treated for a second time with the contrast agent. 30 min later, 2D FLI, 3D FLIT and 2D BLI were performed. After subcutaneous luciferin injection, organs were collected and imaged. This experiment was done in 2017 by Manuela Simlinger. The exact workflow is visualized in Figure 13.

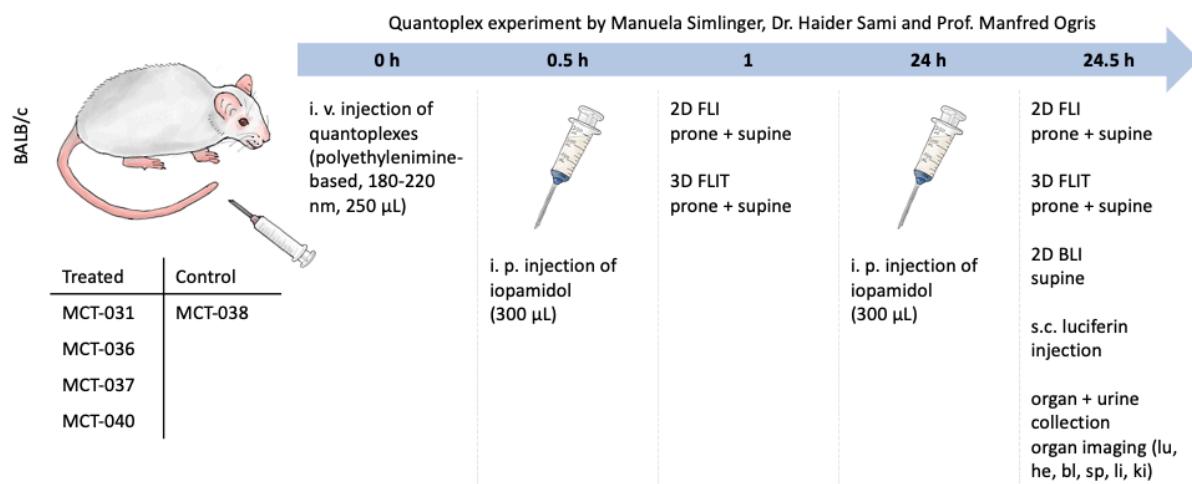


Figure 13: **Workflow and timeline of quantoplex experiment.** MCT-031, MCT-036, MCT-037 and MCT-040 were injected intravenously with quantoplexes. For contrast, mice were injected with iopamidol 30 min before imaging. 1 h and 25.5 h after initial injection mice were images via 2D FLI and 3D FLIT in prone and supine position. At the end of the experiment, mice were injected subcutaneously with luciferin and then the organs were collected and imaged.

### **3. Results**

This chapter presents the main findings gathered during the research of this thesis. As mentioned, this includes the two sections histology and data analysis.

#### **3.1. Histology**

The histological methods include hematoxylin and eosin staining (H&E) and immunohistochemical (IHC) staining of CD90 and firefly luciferase. In the following sections, the obtained images are presented.

##### **3.1.1. Hematoxylin and eosin staining of murine tissue**

Hematoxylin and eosin staining was performed to better visualize the exact cell structures of the organs. To validate the method, the various organ types were each stained at least one for training purposes prior to the real experiments. The staining of brain, tumor and skin is shown exemplarily in Figure 14. These organs were taken from a mouse bearing a B16F10 melanoma. The dense cell composition in the brain facilitated the staining method and makes the neurons with their nuclei clearly visible (Figure 14). In Figure 14 a neuron is marked with an arrow at 400x magnification. In tumor tissue, also melanin accumulation, which is best visible in Figure 14 at 100x magnification and responsible for the characteristic dark pigmentation of tumor cells, was clearly detectable next to tumor cells. Skin tissue showed the highest diversity, since all skin layers, glands and fat could be detected at different localizations. For example, glands are shown in detail in Figure 14. In the lung, alveoli (a) and bronchioli (b) could be detected.

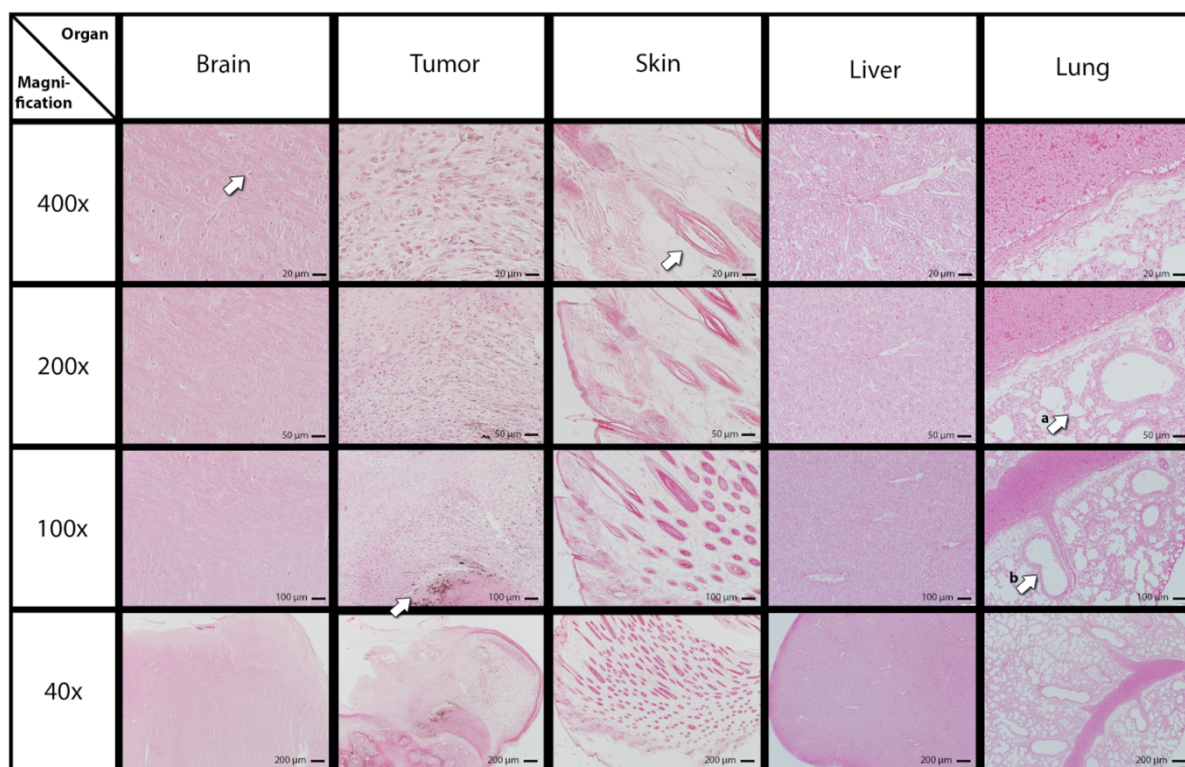


Figure 14: **Hematoxylin and eosin staining of brain, tumor and skin of MCT-180.** Eosin stained cytoplasm pink and hematoxylin stained nuclei dark blue. All pictures of each organ were done with light microscopy at 400-, 200-, 100- and 40-fold magnification (objective magnification, 10x eyepiece). Characteristic structures for every organ were marked by an arrow. In the brain neurons, in tumors melanin and in skin glands were clearly visible. In the lung, alveoli (a) and bronchioli (b) were detectable.

### 3.1.2. Effective CD90 detection via immunohistochemistry

To detect the surface protein CD90, three Thy-1.2-Luc transgenic mice (Figure 15, Figure 16, Figure 17) of the strain CB57/BI6 were injected subcutaneously with  $10^6$  B16F10 melanoma cells. An additional three mice of the same strain served as control wildtype (Figure 18, Figure 19, Figure 20) and were not injected with melanoma cells. All mice were stained immunohistochemically with an anti-CD90 antibody in a 1:600 dilution. For every mouse the organs brain, skin and tumor were stained and images were taken at various magnifications of the bright field microscope (400x, 200x, 100x 40x). As expected, all organs were stained positively. Effective staining could also be confirmed by signals detected in BLI, since CD90 expression occurs together with that of luciferase under the control of the Thy-1.2 expression cassette. The intense positive staining of skin and tumor can be correlated to the luciferase signals detectable in organ images, which could be shown by other students (Merlina Wojta and Aileen Prosche) being specialized in the work with animals. The higher the intensity of brown coloration in IHC, the more CD90 protein was expressed in the organ. According to all conducted stainings, tumor cells were stained most intensively indicating a CD90 overexpression. Also,

this protein was expressed in a high amount in the skin layers, glands and hair follicles. CD90 was also expressed in neurons of the brain, although the brown coloration was not as intense as it was in the other organs. For each staining and organ, a negative control was performed with isotype and buffer to determine unspecific staining. However, all negative controls showed no or little brown staining, which could be neglected.



Figure 15: IHC staining of brain, tumor and skin of Thy-1.2-Luc transgenic mouse MCT-172. Each organ was treated with a primary anti-CD90 antibody in a 1:600 dilution and a secondary antibody. All organs treated with the primary antibody were stained positively. For each organ a negative control was performed with isotype and buffer. Both picture sets of each organ were done with light microscopy at 400-, 200-, 100- and 40-fold magnification (objective magnification, 10x eyepiece) at the same location. **A.** IHC of brain. **B.** IHC of tumor. **C.** IHC of skin.

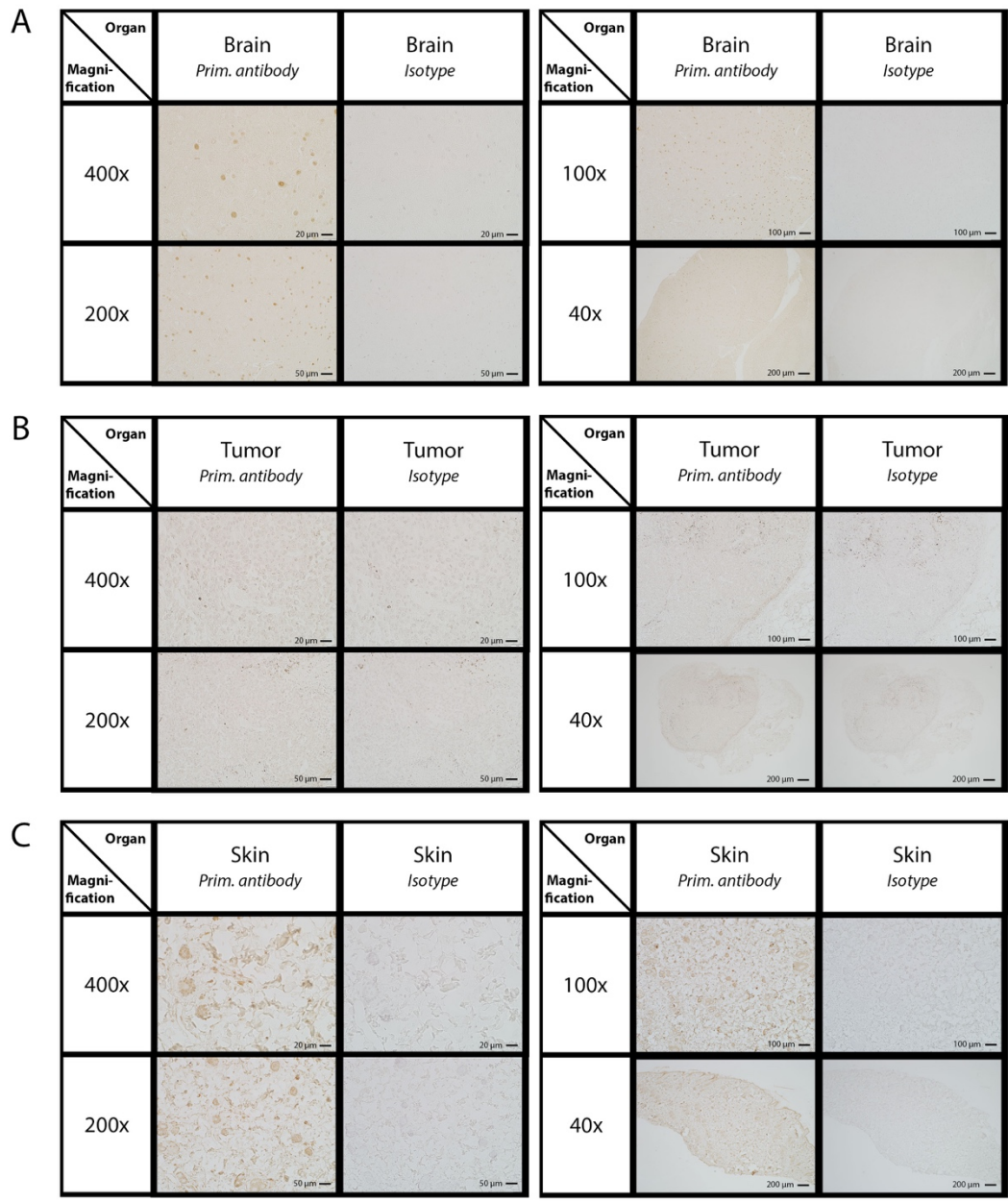


Figure 16: IHC staining of brain, tumor and skin of Thy-1.2-Luc transgenic mouse MCT-173. Each organ was treated with a primary anti-CD90 antibody in a 1:600 dilution and a secondary antibody. All organs treated with the primary antibody were stained positively. Especially the positive staining of neurons in the brain was visible here. Both picture sets of each organ were done with light microscopy at 400-, 200-, 100- and 40-fold magnification (objective magnification, 10x eyepiece) at the same location. **A.** IHC of brain. **B.** IHC of tumor. **C.** IHC of skin.

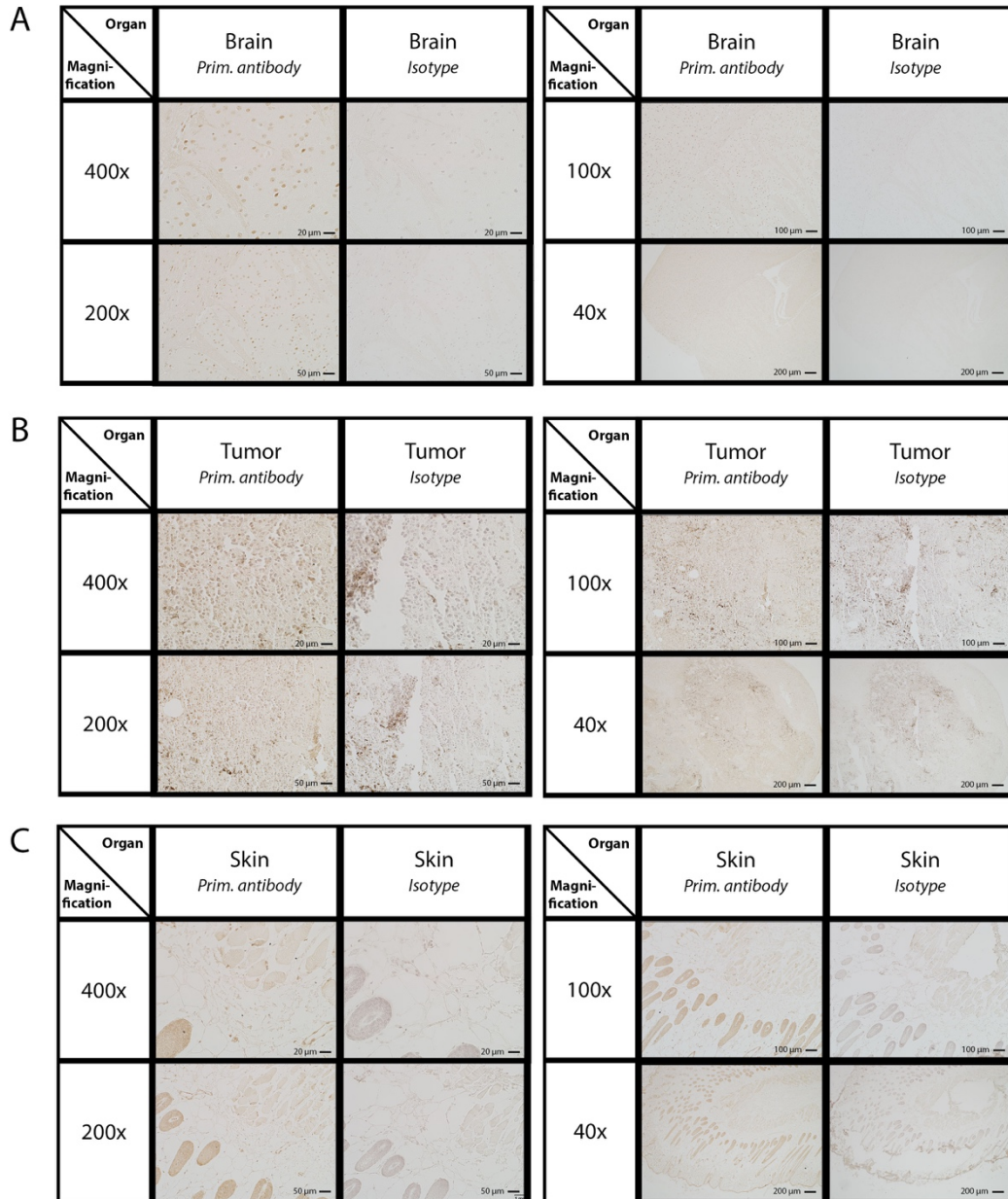


Figure 17: IHC staining of brain, tumor and skin of Thy-1.2-Luc transgenic mouse MCT-179. Each organ was treated with a primary anti-CD90 antibody in a 1:600 dilution and a secondary antibody. All organs treated with the primary antibody were stained positively. Especially the positive staining of neurons in the brain, of tumor cells and glands in the skin was visible here. Both picture sets of each organ were done with light microscopy at 400-, 200-, 100- and 40-fold magnification (objective magnification, 10x eyepiece) at the same location. **A.** IHC of brain. **B.** IHC of tumor. **C.** IHC of skin.

As control, wildtype mice of the strain CB57BL/6 without being treated with melanoma cells were stained to test them for positive staining. Positive staining of these organs was similar to that of Thy-1.2-Luc transgenic mice, as expected.

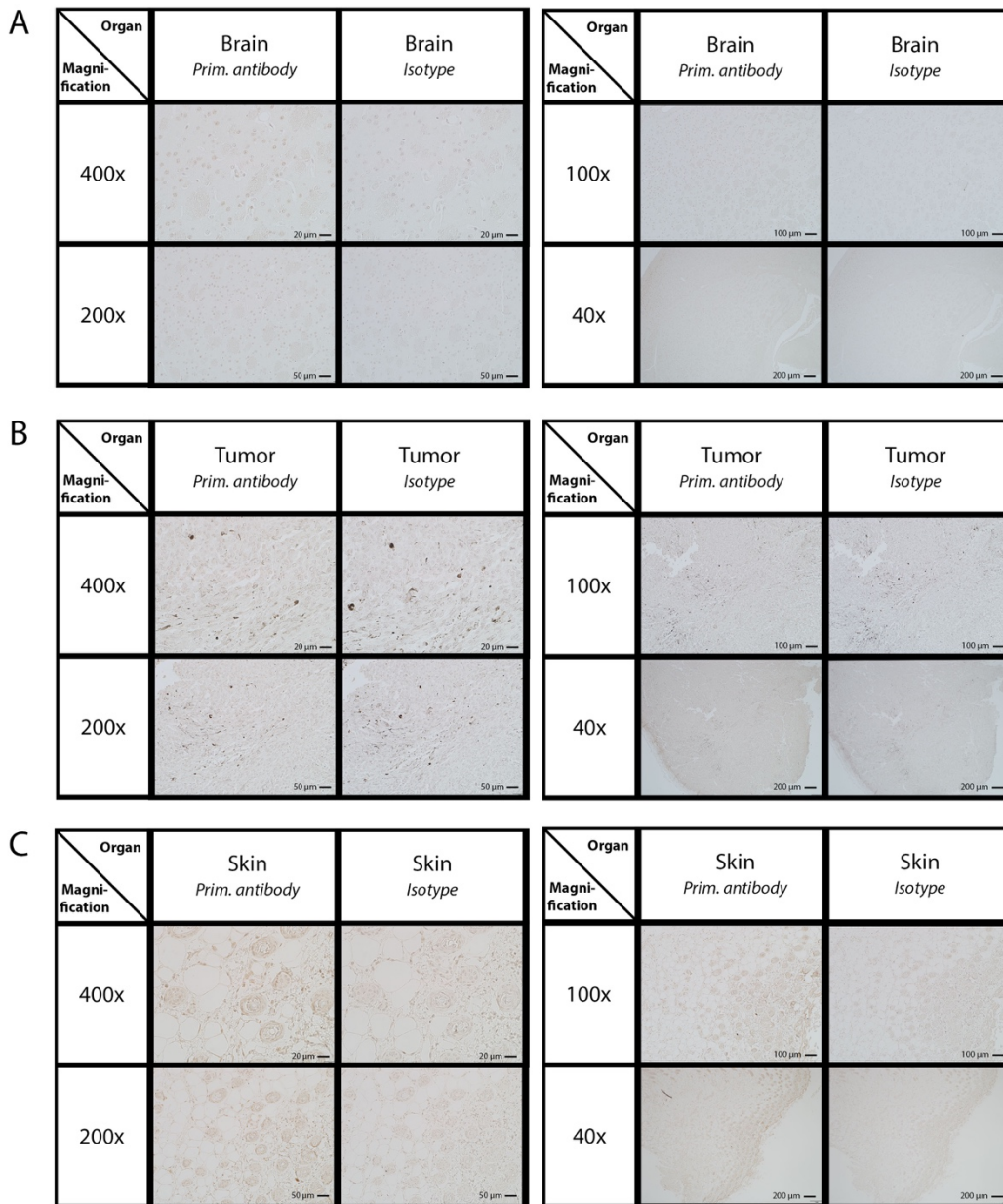


Figure 18: IHC staining of brain, tumor and skin of wild type mouse MCT-356. Each organ was treated with a primary anti-CD90 antibody in a 1:600 dilution and a secondary antibody. All organs treated with the primary antibody were stained positively. Both picture sets of each organ were done with light microscopy at 400-, 200-, 100- and 40-fold magnification (objective magnification, 10x eyepiece) at the same location. **A.** IHC of brain. **B.** IHC of tumor. **C.** IHC of skin.

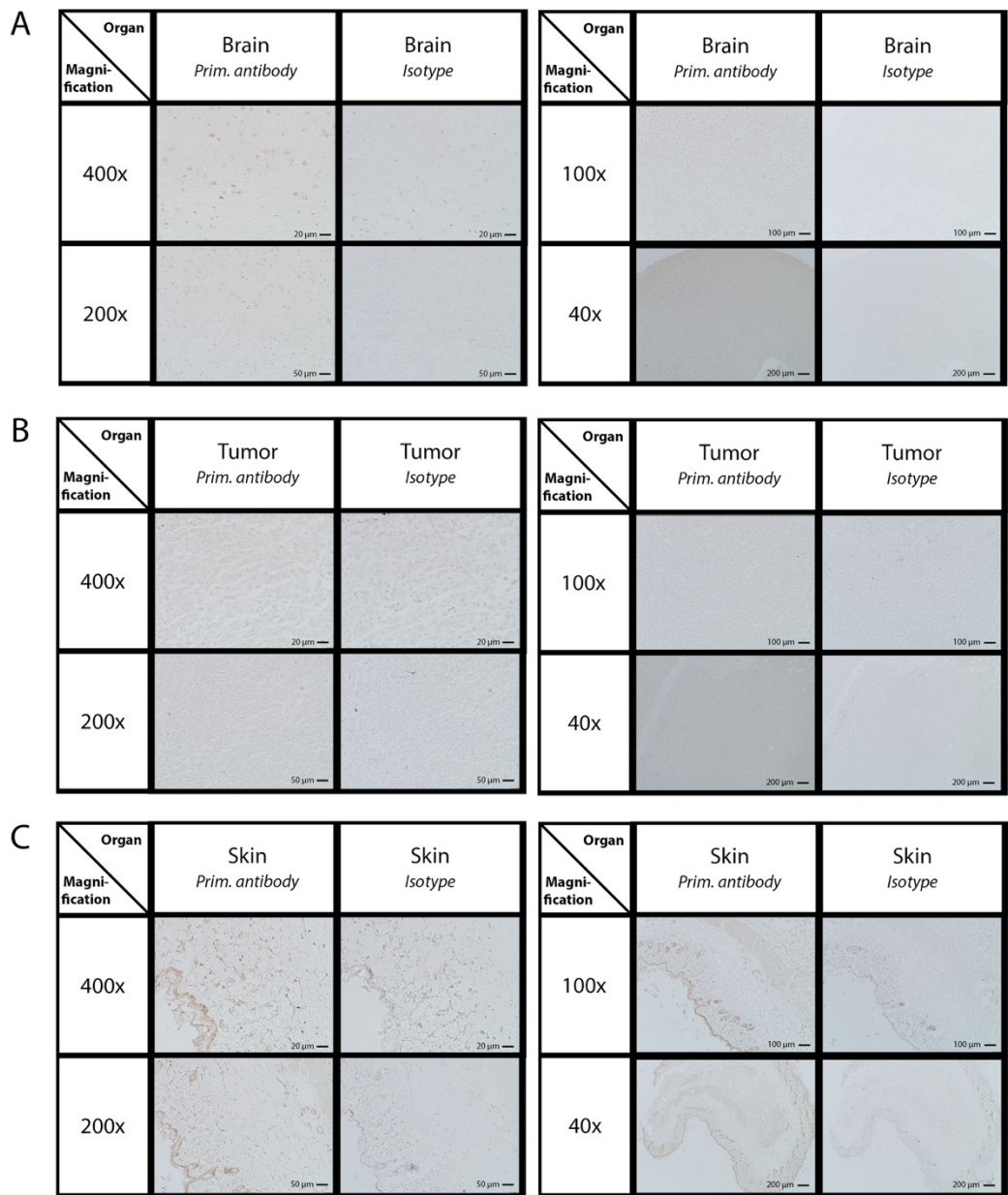


Figure 19: IHC staining of brain, tumor and skin of wildtype mouse MCT-357. Each organ was treated with a primary anti-CD90 antibody in a 1:600 dilution and a secondary antibody. All organs treated with the primary antibody were stained positively. Both picture sets of each organ were done with light microscopy at 400-, 200-, 100- and 40-fold magnification (objective magnification, 10x eyepiece) at the same location. **A.** IHC of brain. **B.** IHC of tumor. **C.** IHC of skin.

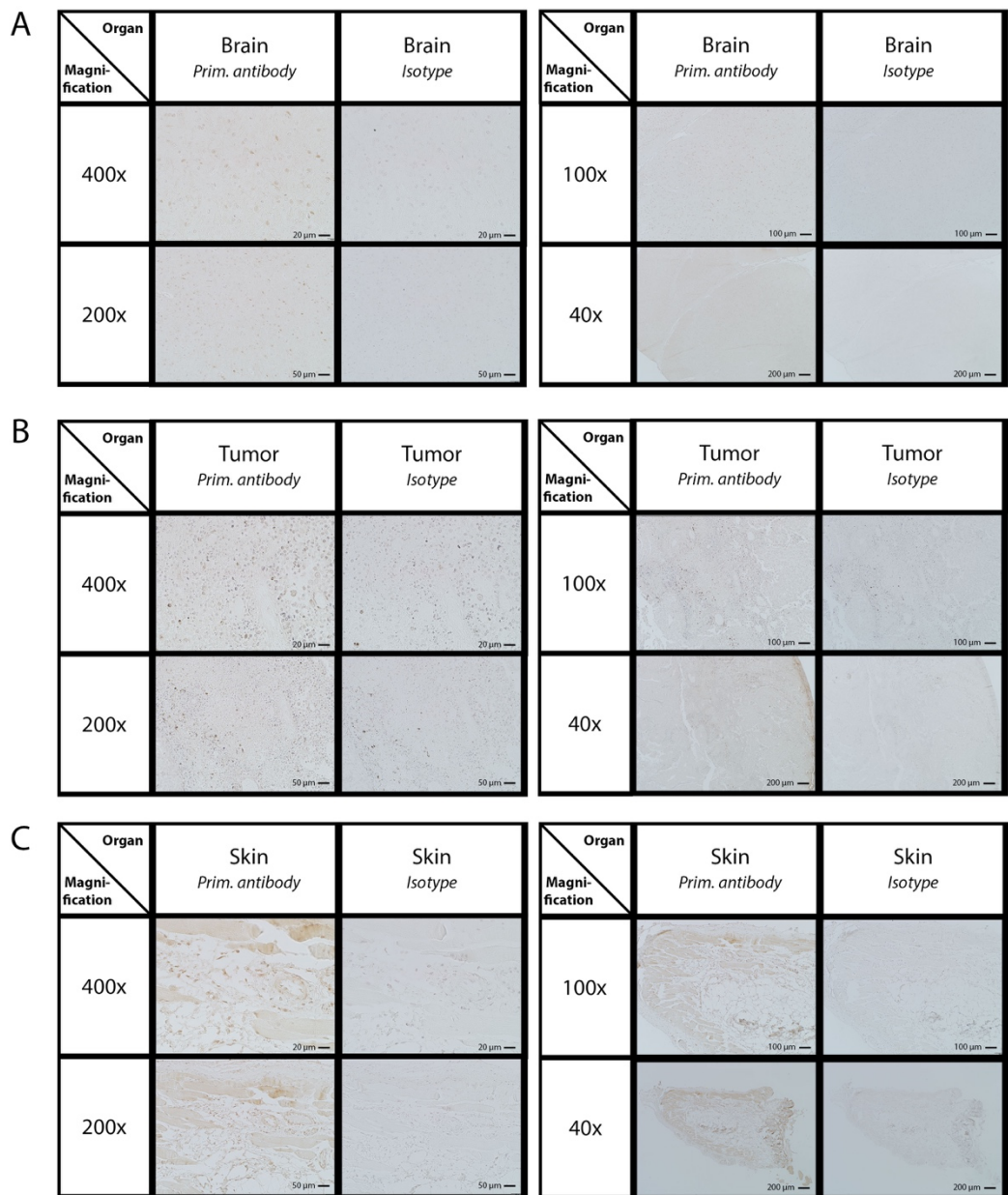


Figure 20: IHC staining of brain, tumor and skin of wildtype mouse MCT-358. Each organ was treated with a primary anti-CD90 antibody in a 1:600 dilution and a secondary antibody. All organs treated with the primary antibody were stained positively. Both picture sets of each organ were done with light microscopy at 400-, 200-, 100- and 40-fold magnification (objective magnification, 10x eyepiece) at the same location. **A.** IHC of brain. **B.** IHC of tumor. **C.** IHC of skin.

### 3.1.3. Firefly luciferase detection via immunohistochemistry

In order to have a positive control for luciferase staining, two BALB/c mice bearing 4T1 tumors in their lungs were stained. One mouse (M-106) was used as positive control (4T1-Luc tumor cells, stably expressing firefly luciferase, and one (M-113) with 4T1 tumors expressing the near infrared fluorescent protein iRFP720 [67] (Table 5). For detection of luciferase, immunohistochemistry was performed with a primary goat antibody to firefly luciferase in a 1:1000 dilution. In mouse M-106, some parts with positive staining in the lung were observed, indicating that luciferase is expressed in this area, which was marked by an arrow in Figure 21 (M-106). In the lung of the other mouse (M-113) no positive staining could be detected. For illustration, positive staining of the lung from M-106 (of the type #1\_4T[PE]Luc) is directly compared to negative staining of the lung from M-113 in Figure 21. As it was done for CD90 staining, organs were stained and imaged at various magnifications with the bright field microscope. Also, negative controls were performed using an isotype control as primary antibody. In this experiment, the negative stained organs, respectively parts of the organs have the same color as the negative controls.

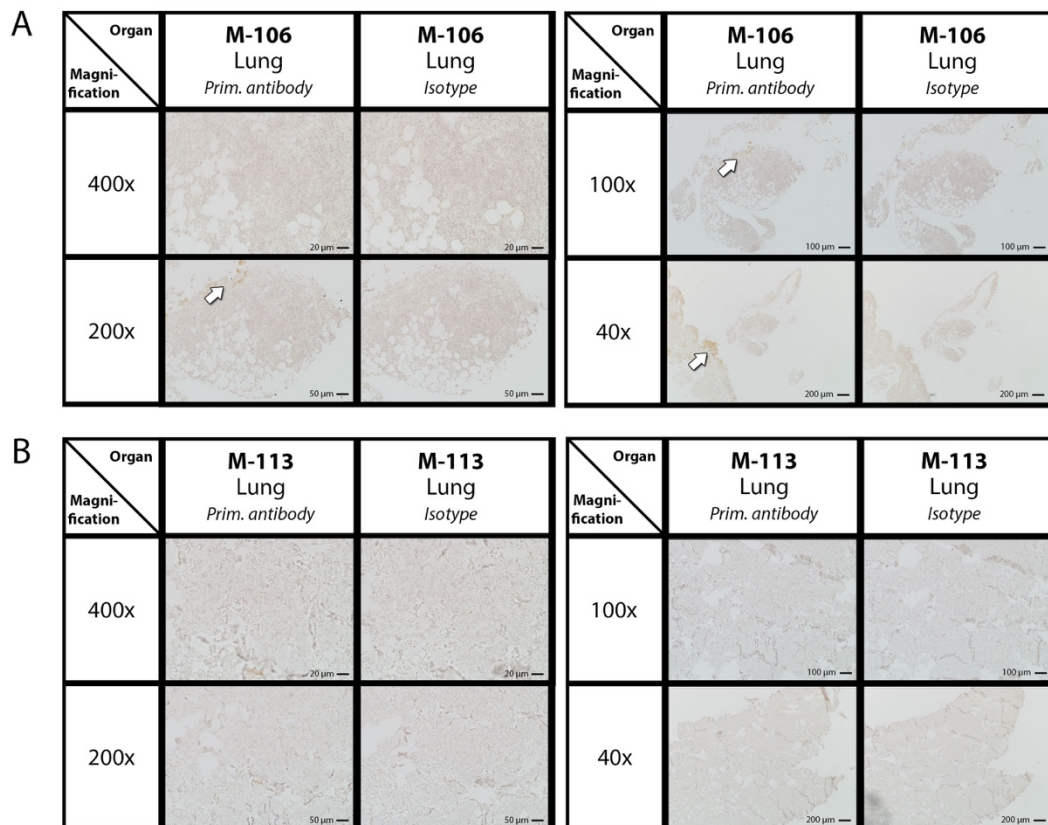


Figure 21: **Detection of luciferase in the lung via IHC.** **A.** IHC of M-106 (#1\_4T[PE]Luc). A part with positive staining could be detected in the lung (marked by arrows). **B.** IHC of M-113. As comparison, M-113 did not show any positive staining in the lung.

## **3.2. Fluorescence tomography data analysis**

3D FLIT analysis was performed to track the biodistribution of naked siRNA and other nanoparticles. Especially, tracking of naked siRNA-AF750, auropolyplexes loaded with siRNA-AF750, quantum dots and quantoplexes were performed. All of these nanoparticles show different biodistribution of the signals and different delivery efficiency.

### **3.2.1. Influence of changing threshold values on FLIT measurements**

To make sure that whole data analysis and subsequent measurements of ROIs are reproducible, it was firstly determined whether changing the background signal and its corresponding threshold value influence the measurement of ROIs. For this, data of a representative mouse (MCT-015) treated with auropolyplexes loaded with siRNA-AF750 was analyzed. For this experiment, 637 pmol AF750 dye were injected into every mouse. To prove that the measurement does not depend on the chosen threshold value, analysis was done once without changing the scale, once with logarithmic scale, but not changing the threshold value, and once with logarithmic scale and adjusted threshold value (Figure 22A). Measurements were taken with default and adjusted threshold values at logarithmic scale at two different moments (0 h, 24 h) for comparison. As seen in Figure 22B, changing the threshold value had no influence on measurements. The values for data with default threshold and adjusted threshold were exactly the same, indicating that threshold values have no influence on the measurement of ROIs. Decreasing the threshold value reduced background signal, which was visible as blue cloudy structures. With decreased background signal, view can be focused more on relevant signal. With the logarithmic scale, signal appeared with more color intensity and brightness, compared to the raw image.

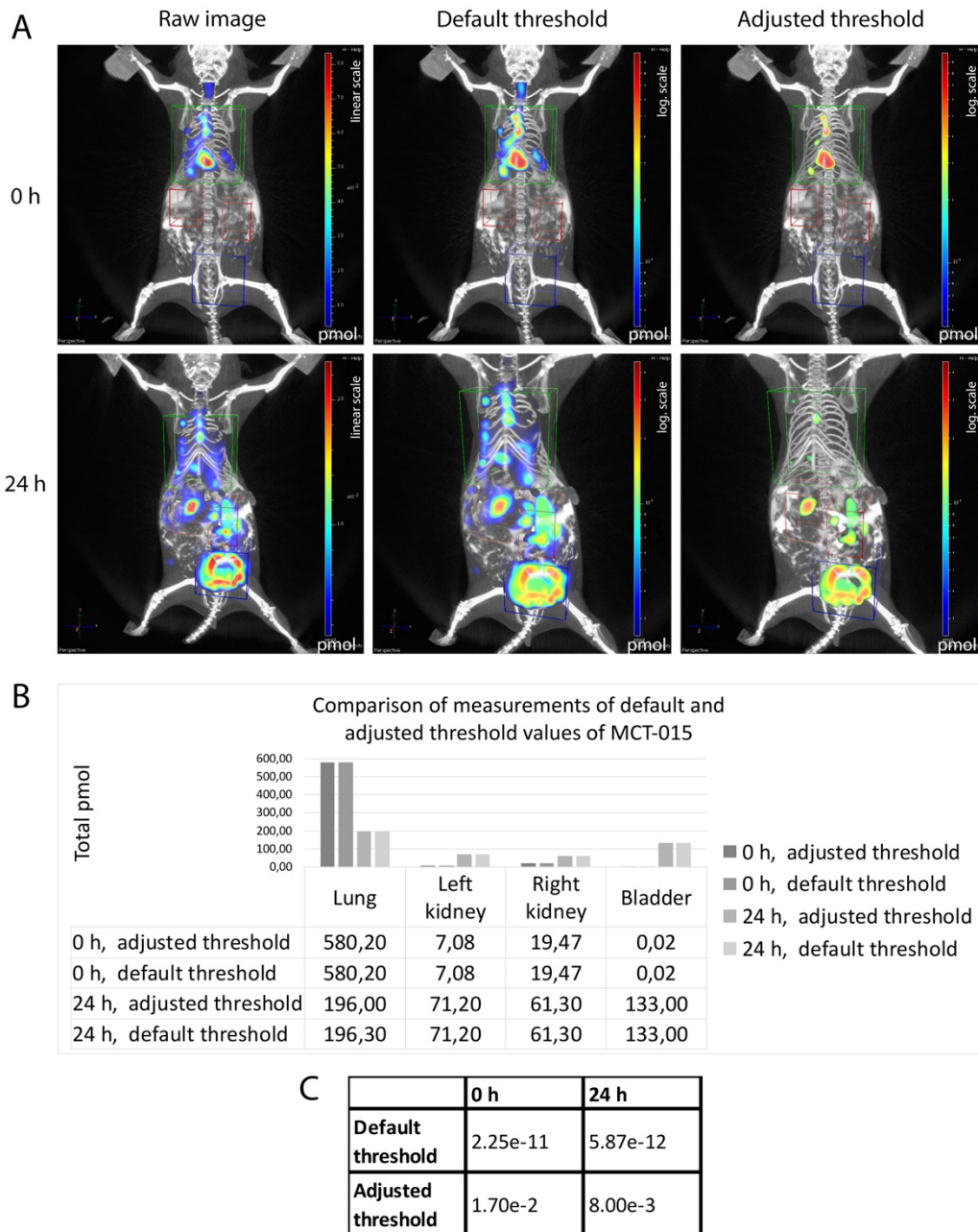
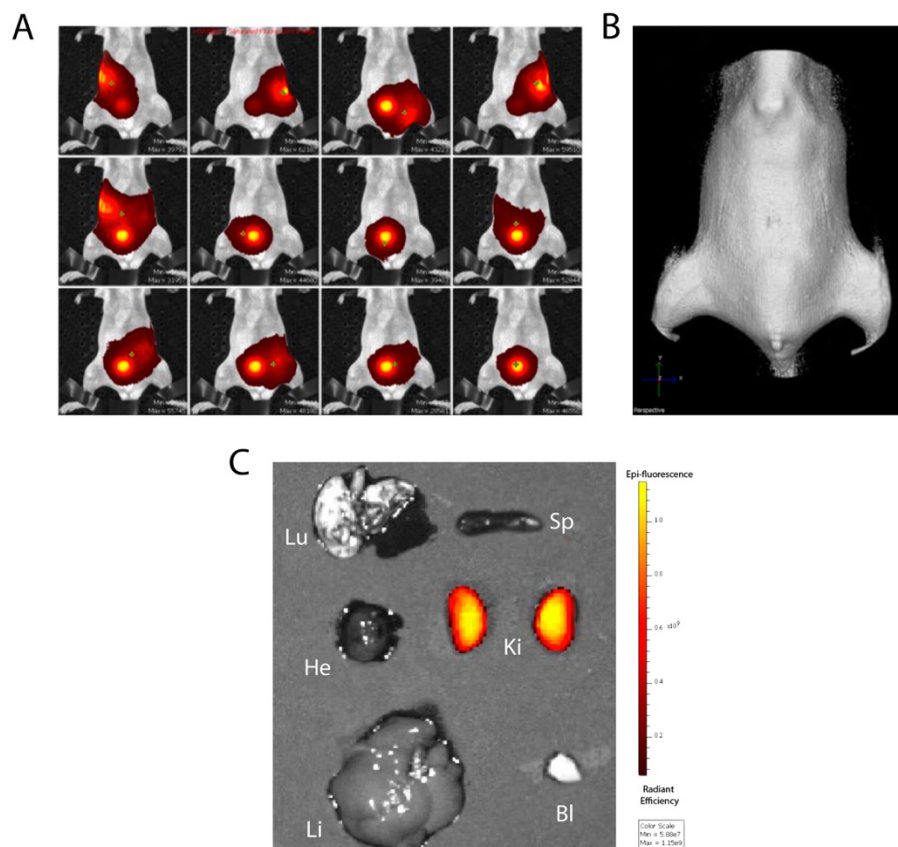


Figure 22: **Effect of default and adjusted threshold values on ROI measurement for 3D FLIT analysis.** **A.** The images on the left show raw images, which were taken without making any adjustments. In the image in the middle, logarithmic scale was set, but no changes in threshold values were done. In the images on the right, logarithmic scale was set and threshold was decreased. **B.** Comparison of measurements with adjusted and non-adjusted threshold. Measurement values of images with adjusted and default threshold values were identical. **C.** Default and adjusted threshold values in numbers.

### 3.2.2. Tracking biodistribution of naked siRNA-AF750 after systemic administration

To measure biodistribution of siRNA-AF750, B6 Albino CR mice were injected intravenously with siRNA labelled with AF750 (in total 1274 pmol dye/mouse). For better CT images, the contrast agent iopamidol was added intraperitoneally. For this experiment, three mice (MCT-

361, MCT-362, MCT-363) were analyzed by 3D FLIT imaging. The control mice (MCT-364, MCT-365) were not analyzed by FLIT, but they were used for organ analysis. As visible in Figure 23D, all of the treated mice showed similar results in signal intensity. For better visualization and the reason explained in the section above, only images with adjusted threshold values at logarithmic scale (Figure 24A-C) are shown. The first step of 3D FLIT analysis was to load 2D fluorescence pictures (Figure 23A). Here, the fluorescence was recorded in color-coded transillumination overlaid by a reflected light picture. The green dots in the middle of the image depicted the position of the transillumination light source, which was arranged as explained in the introduction (Figure 8). The picture in Figure 23B shows the mouse topography of reconstructed CT data. The *ex vivo* 2D epi-fluorescence FLI organ images showed a high AF750 content in kidneys 24 h after injection (Figure 23C). The other organs shown exhibit only the background signal, which was reduced for better visualization.



**Figure 23. 3D signal reconstruction and 2D epifluorescence FLI organ imaging of naked siRNA-AF750.** C57BL/6 albino mice were injected intravenously with siRNA-AF750 and with iopamidol intraperitoneally. **A.** 2D fluorescence pictures. Fluorescence was recorded in color-coded transillumination overlaid by reflected light picture. The green dots depicted in every image represent the position of the transilluminating light source. **B.** Topography of reconstructed CT data. **C.** *Ex vivo* 2D epi-fluorescence FLI images. High AF750 amounts were detected in the kidneys. The signal was color coded: highest signal intensity was shown in yellow, whereas lowest intensity was shown in red.

To determine biodistribution of siRNA-AF750, cuboid ROIs were drawn individually for each organ and mouse in dorsal position considering that each ROI should have approximately the same volume per organ. The biodistribution of AF750 amount was observed once immediately after siRNA-AF750 injection and once 24 h later. The left part (0 h) of Figure 24A-C showed FLIT signal distribution immediately after siRNA-AF750 injection. Here, the highest AF750 amount was detected in the bladder. As seen in Figure 24D, both kidneys also showed signal, but significantly less than the bladder did initially. According to the right side of Figure 24A-C, which depicts signal distribution after 24 h, no signal could be detected in the bladder and signal intensity of the kidneys decreased by approximately 50% compared to the initial signal intensity detected in the kidneys. All three tested mice showed similar biodistribution behavior over experimental time. However, when comparing the FLIT images of 0 h and 24 h, it should be considered that they did not have the same scale because no good visualization was possible this way.

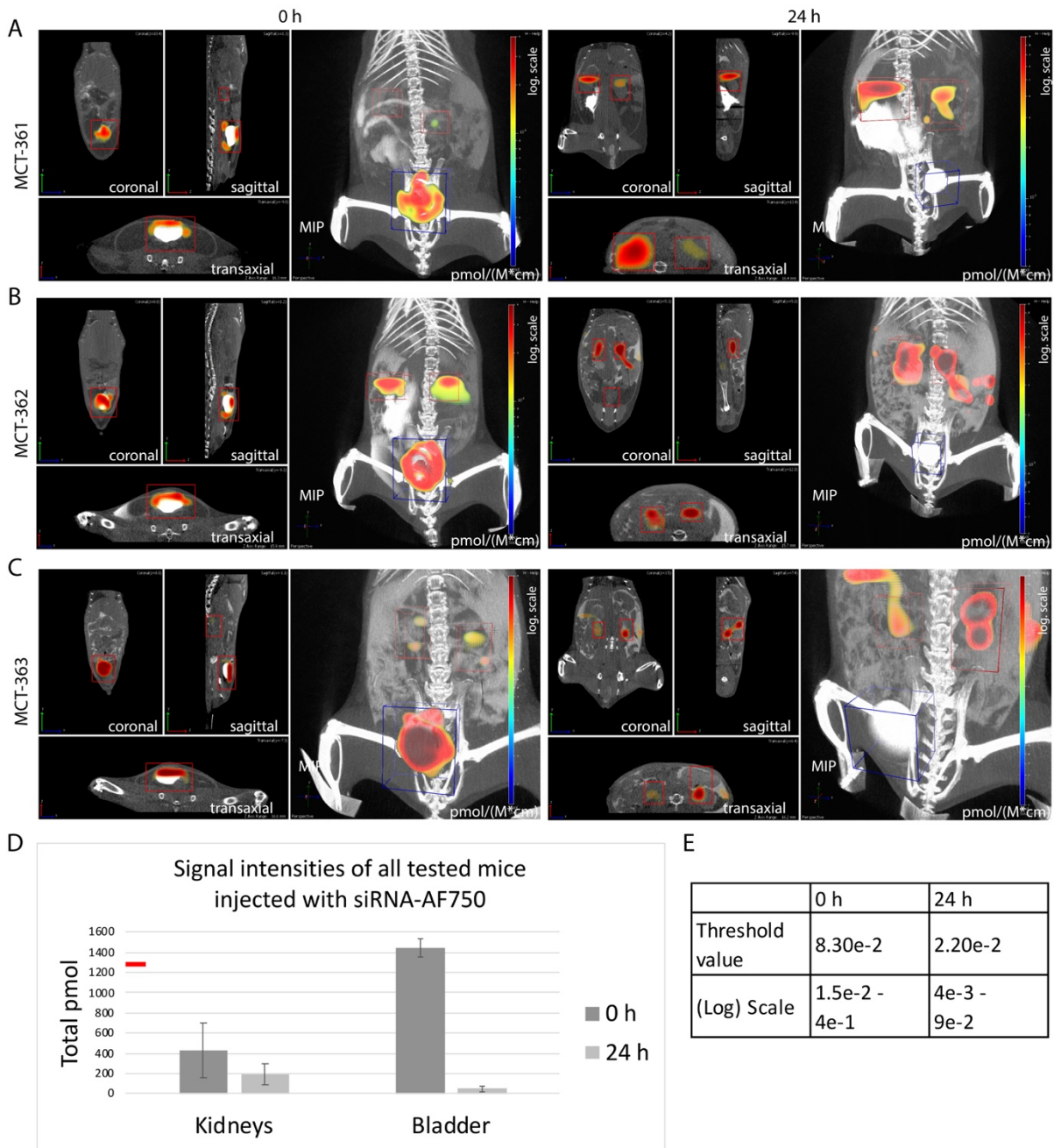


Figure 24: **3D FLIT signal distribution of naked siRNA-AF750 after 0 h and 24 h.** FLIT images showed all planes on the left (coronal, sagittal, transaxial) and the maximum intensity projection (MIP) on the right. The signal was color coded: highest signal intensity was shown in red, whereas lowest intensity was shown in blue. Initial signal (0 h, left) was detected in the bladder and both kidneys. After 24 h (right), no signal was detected in the bladder and signal intensity in the kidneys decreased by the half. **A.** MCT-361. **B.** MCT-362. **C.** MCT-363. **D.** Average signal intensities with corresponding standard deviations of all three tested mice summarized in one graph. The AF750 content was measured in total pmol (n=3, +/- standard deviation). The red line marks the initial amount of AF750 (1274 pmol) applied to each mouse. Kidney signal represented the average signal of both kidneys. **E.** Uniform values for adjusted threshold and scale for each 0 h and 24 h.

### **3.2.3. Tracking biodistribution of siRNA-AF750 based auropolyplexes after systemic administration**

The biodistribution of auropolyplexes loaded with siRNA-AF750 (637 pmol AF750 per mouse) was analyzed for three mice (AGE-269, MCT-012, MCT-015). Auropolyplexes were administered intratracheally and iopamidol, which was used as contrast agent, was injected intraperitoneally. As seen on the left side of Figure 25A-C, which shows all images immediately after administration, the initial amount of auropolyplexes loaded with siRNA-AF750 accumulated in the lung. In other organs, no or very low and neglectable signal was detectable immediately after administration. However, compared to the initial signal, lung signal decreased by more than half after 24 h, which is shown on the right side of Figure 25A-C. At this time, signal could be detected also in both kidneys and the bladder. Here it should be considered that the total kidney signal was calculated as an average of the signal of both kidneys (Figure 25D).

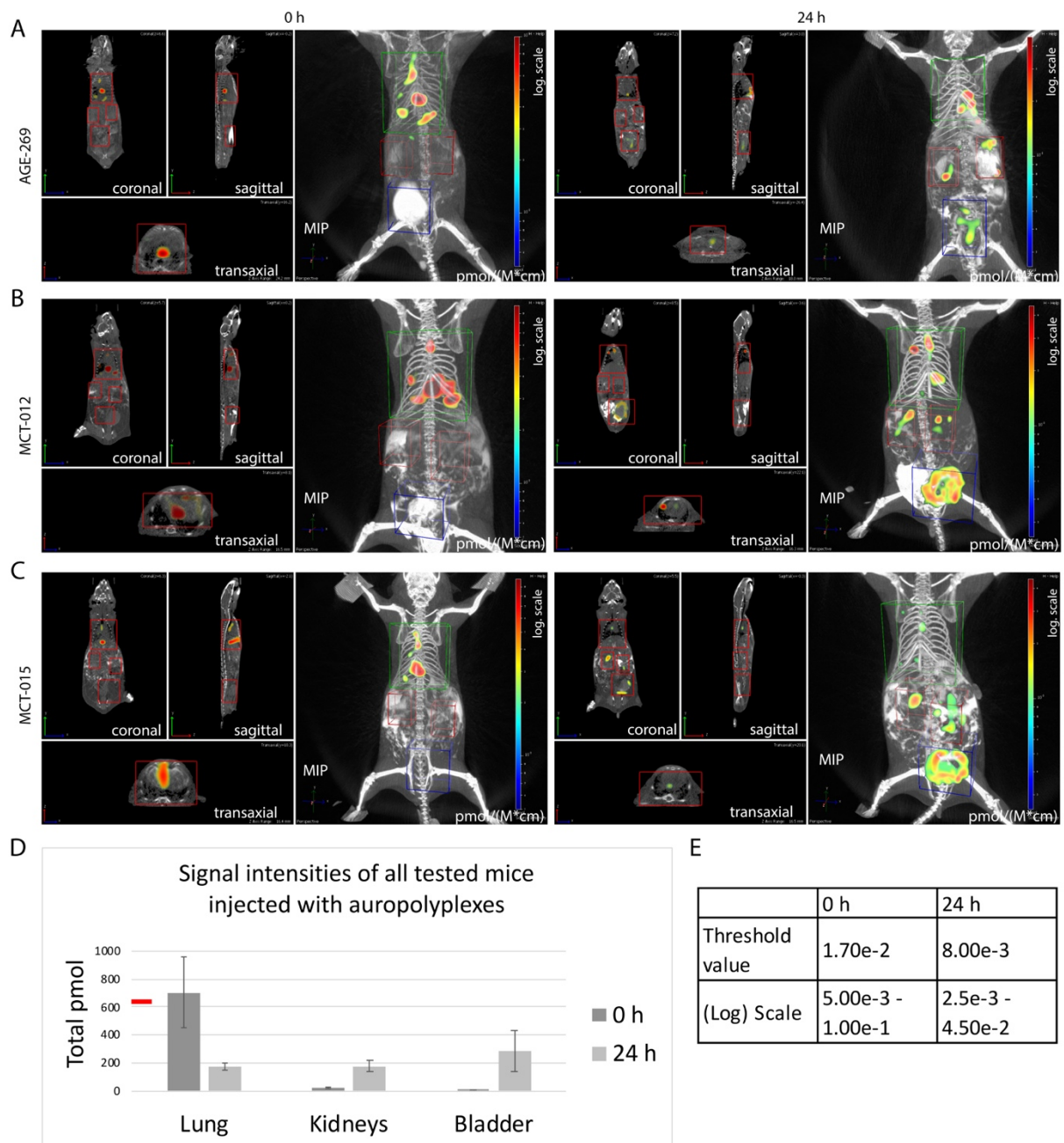


Figure 25: **3D FLIT signal distribution of auropolyplexes loaded with siRNA-AF750 after 0 h and 24 h.** FLIT images showed all planes on the left (coronal, sagittal, transaxial) and the maximum intensity projection (MIP) on the right. The signal was color coded: highest signal intensity was shown in red, whereas lowest intensity was shown in blue. Initial signal (0h, left) was detected in the lung, the other organs showed no relevant signal directly after injection. After 24 h (right), the highest signal was detected in the bladder. Lung signal decreased by more than half. **A.** AGE-269. **B.** MCT-012. **C.** MCT-015. **D.** Average signal intensities with corresponding standard deviations of all three tested mice summarized in one graph. The amount of auropolyplexes was measured in total pmol (n=3, +/- standard deviation). The red line marks the initial amount of AF750 (637 pmol) applied to each mouse. Kidney signal represented the average signal of both kidneys. **E.** Uniform values for adjusted threshold and scale for each 0 h and 24 h.

### **3.2.4. Tracking quantum dot biodistribution after systemic administration**

Cadmium telluride (CdTe) quantum dots with a diameter of 4 nm were injected intravenously into the tail vein of three different mice (MCT-038, PRI-242, PRI-250) of the strain BALB/c. Quantum dots were injected at a dose of 6.9 mg cadmium per kg per mouse. As seen on the left side (0 h) of Figure Figure 26A-C, initial quantum dot signal was detected in the lungs and the liver in all mice. MCT-038 could have some signal on top of the kidneys (Figure 26D) and PRI-250 also seemed to have kidney signal. PRI-242, however, did not show any kidney signal at no measured moment. The signal after 24 h, which is shown on the right side of Figure 26A-C, was similar to that at 0 h, but with weaker intensity. Figure 26E shows the signal intensities of quantum dots in numbers. When comparing data of 0 h and 24 h of this graph, it can be seen that most quantum dots were redistributed within 24 h.

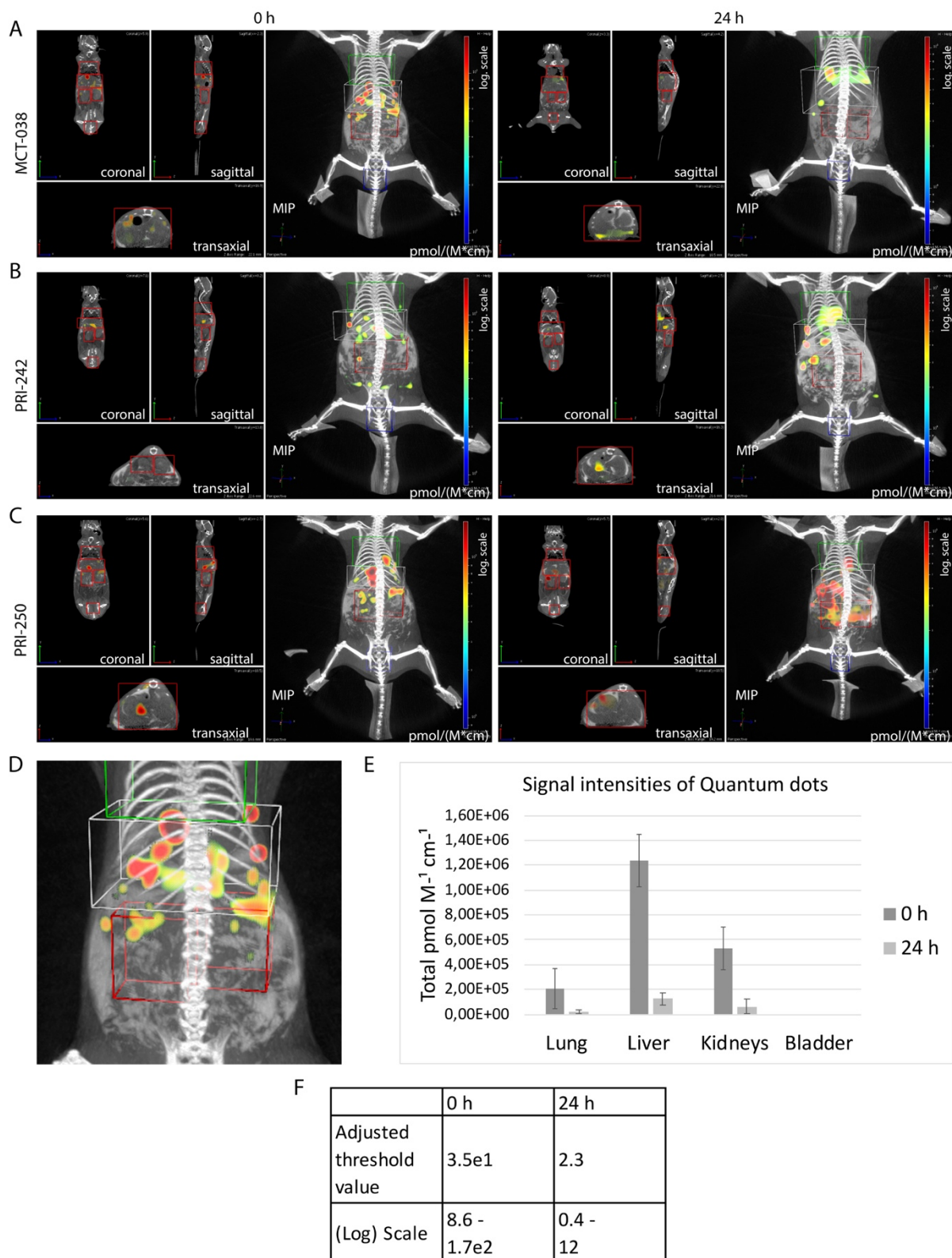


Figure 26: **3D FLIT signal distribution of quantum dots 0 h and 24 h after injection.** FLIT images showed all planes on the left (coronal, sagittal, transaxial) and the maximum intensity projection (MIP) on the right. The signal was color coded: highest signal intensity was shown in red, whereas lowest intensity was shown in blue. All mice comprised liver and lung signal at all analyzed times. **A.** MCT-038 could have signal on top of kidney. **B.** PRI-242 seemed to have no kidney signal. **C.** PRI-250 comprised kidney signal. **D.** Zoomed picture of supposed kidney signal of MCT-038. **E.** Average signal intensities with corresponding standard deviations of all three tested mice summarized in one graph. The signal intensity of quantum dots was measured in total pmol M<sup>-1</sup> cm<sup>-1</sup> (n=3, +/-

standard deviation). Kidney signal represented the average signal of both kidneys. **F.** Uniform values for adjusted threshold and scale for each 0 h and 24 h.

According to *ex vivo* 2D epifluorescence FLI images of organs (Figure 27), signal could be definitely detected in the lungs and liver. Also kidneys showed signal. However, calculation of background signal was based on organ images from Aileen Prosche, another diploma student, because for this project no control organs were available. To calculate the average threshold, the visible background of the control organ images (MCT-410, MCT-407) (Figure 27A) was totally reduced. Ideally, signal is visible then in the images showing treated organs (MCT-406, MCT-409) on the left. The average threshold of these images was taken to reduce the background of the organ images of this project. For all three mice signal could be detected in the liver and the lungs. PRI-242 and PRI-250 also showed weak signal in the kidneys. (Figure 27B).

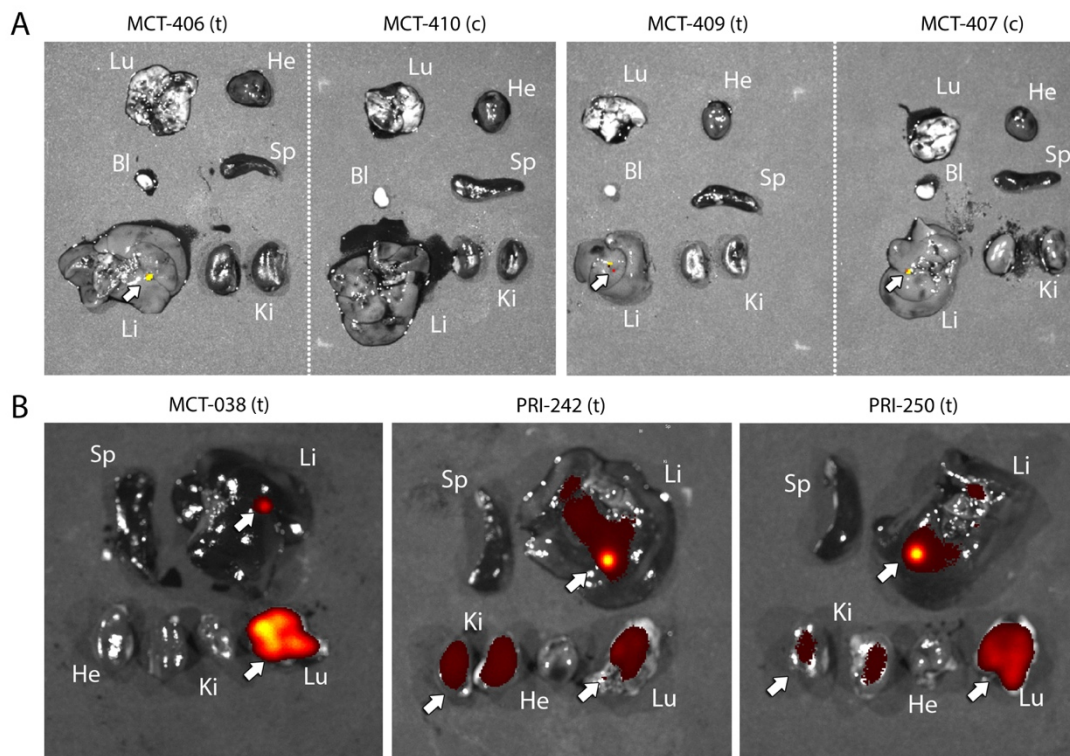


Figure 27: **Ex vivo epifluorescence FLI organ images of quantum dots experiments.** **A.** Organ images of quantum dot experiment from AP/FA. Average threshold of these images was calculated. **B.** Organ images of quantum dot experiment from this project. The average threshold of the images above was used to reduce visible background. In MCT-038 signal was detected in liver and lungs. In PRI-242 and PRI-250 signal was detected in liver, lungs and kidneys.

### **3.2.5. Tracking quantoplex biodistribution after systemic administration**

Polyethylenimine (PEI)-based quantoplexes with a diameter of 180-220 nm were injected intravenously into the tail vein of four different mice (MCT-031, MCT-037, MCT-040, MCT-036) of the strain BALB/c. Quantoplexes contained NIR-emitting quantum dots having a size of 4 nm and containing 17.26  $\mu\text{g}$  of cadmium. MCT-040 was analyzed, but not shown because some data points were missing. Immediately after quantoplex injection, all mice showed signal in mainly lungs and liver, but also weakly in kidneys and bladder, which can be seen on the left side of Figure 28A-C and in the exemplarily zoomed picture of MCT-037 in Figure 28D. 24 h after injection, which is depicted on the right side of Figure 28A-C, signal distribution was similar to that after 0 h, except that total signal decreased by approximately half. Data of decreased signal can be taken in numbers from the graph of Figure 28E.

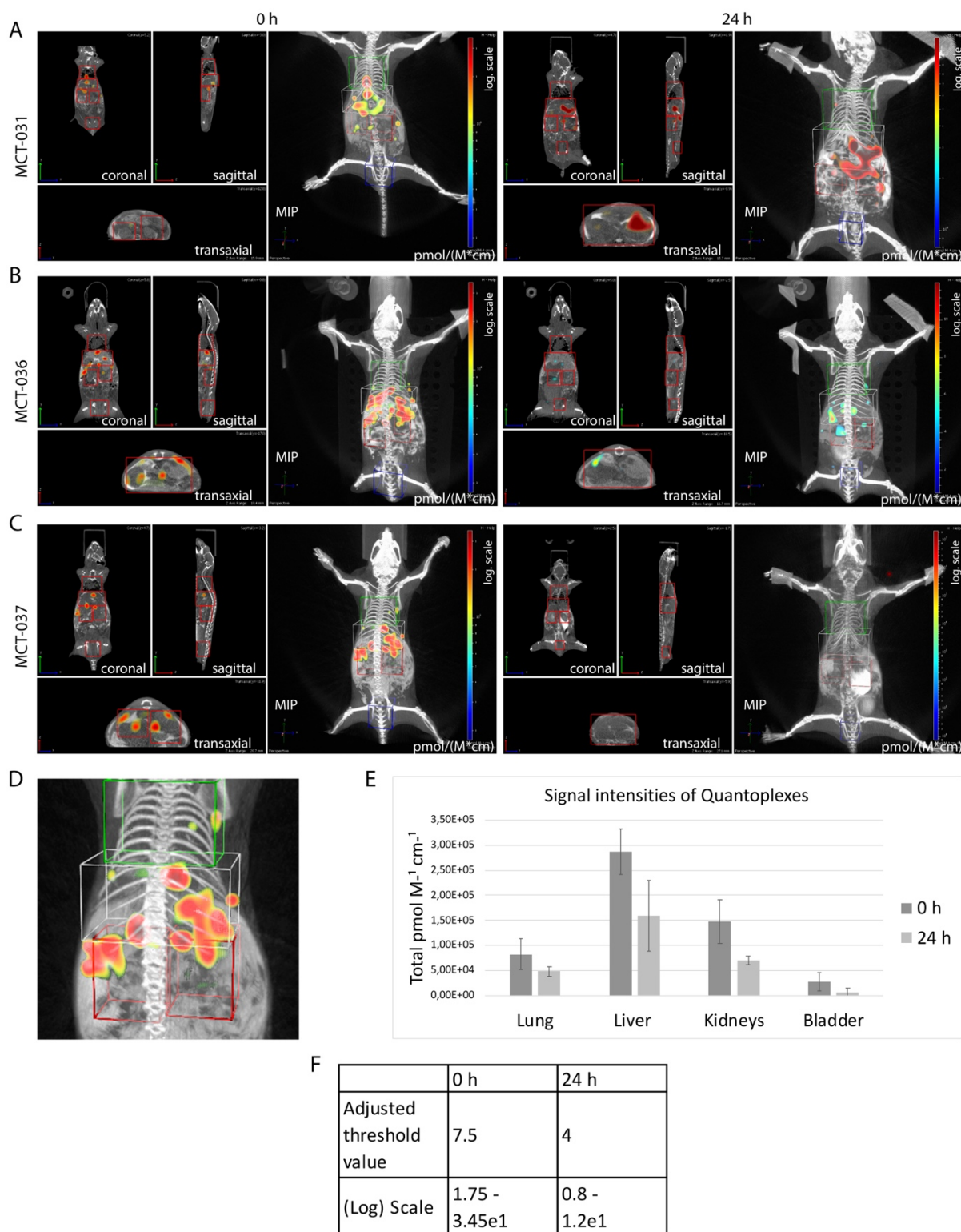


Figure 28: **3D FLIT signal distribution of quantoplexes 0 h and 24 h after injection.** FLIT images showed all planes on the left (coronal, sagittal, transaxial) and the maximum intensity projection (MIP) on the right. The signal was color coded: highest signal intensity was shown in red, whereas lowest intensity was shown in blue. All mice showed signal in the liver and lungs at all analyzed times. In the other organs only weak and neglectable signal was detected. **A.** MCT-031. **B.** MCT-036. **C.** MCT-037. 24h after injection no signal was available. **D.** Zoomed picture of supposed kidney signal of MCT-037. **E.** Average signal intensities with corresponding standard deviations of all three tested mice summarized in one graph. The signal intensity of quantoplexes was measured in total pmol M<sup>-1</sup>

cm<sup>-1</sup> (n=3, +/- standard deviation). Kidney signal represented the average signal of both kidneys. F. Uniform values for adjusted threshold and scale for each 0 h and 24 h.

Threshold calculation of organ images of quantoplexes was performed similarly based on another quantoplex experiment by Patricia Gabler, since no control organ images were available for this experiment. Therefore it is possible, that the chosen threshold value to adjust background signal was not totally accurate. Also, organ images were available for only two out of three mice analyzed by 3D FLIT. Organ images of MCT-036 and MCT-040 were missing. To calculate the average threshold, the visible background signal of the control organ images (MCT-300, MCT-154, MCT-157) of Figure 29A was reduced manually. Ideally, signal was visible then in the images showing treated organs (MCT-101, MCT-301, MCT-352) on the left. The average threshold of these images was taken to reduce the background of organ images from this project shown (Figure 29B). According to these *ex vivo* 2D epifluorescence FLI organ images, signal could be definitely detected in lungs and liver of all analyzed mice (MCT-031, MCT-037). There was also high signal detected in the stomach, which was autofluorescence occurring due to filter paired images.

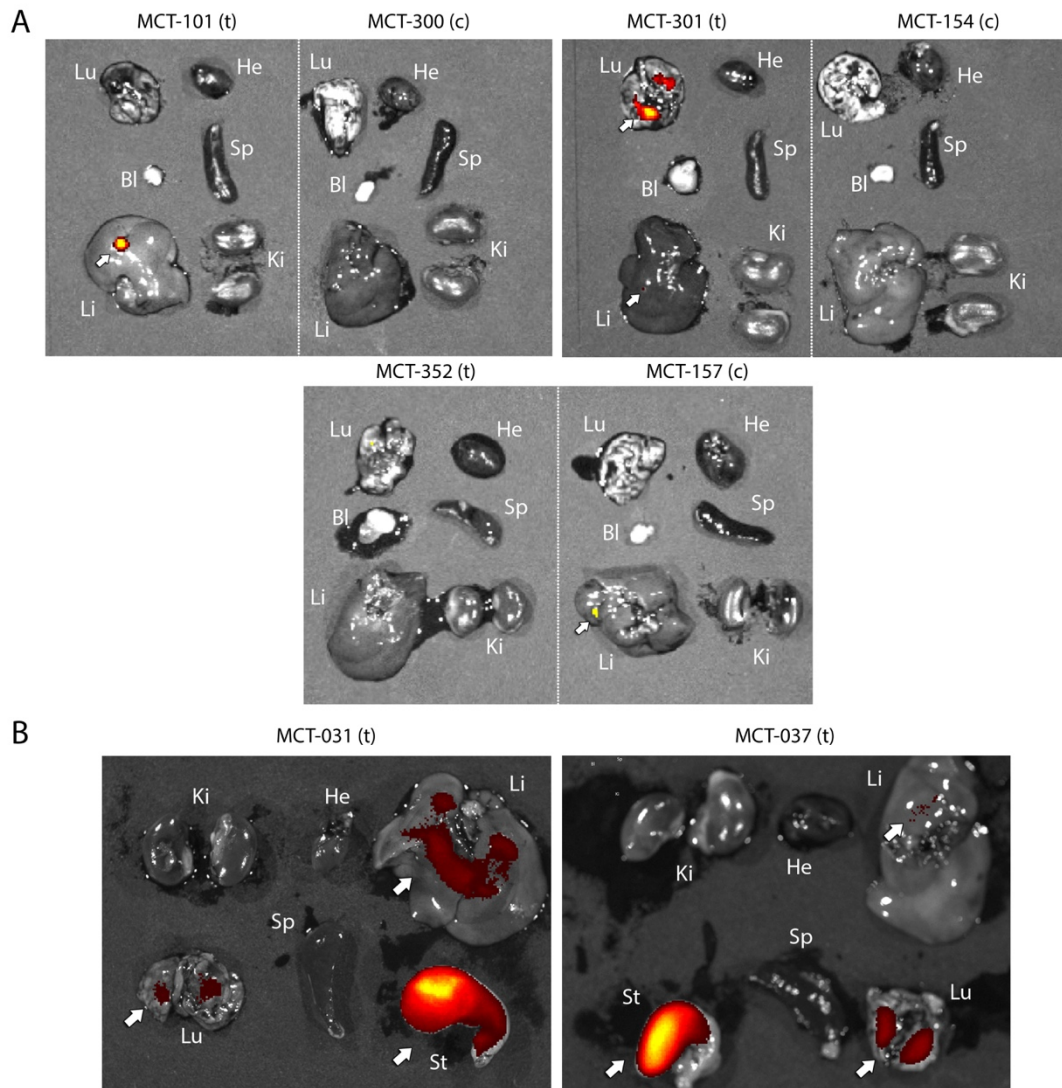


Figure 29: **Ex vivo epifluorescence FLI organ images of quantoplex experiment.** **A.** Organ images of quantoplex experiment from PG/FA. Average threshold of these images was calculated. **B.** Organ images of quantoplex experiment from this project. The average threshold of the images above was used to reduce visible background. All mice comprising organ images showed signal in lungs, liver and stomach. Stomach signal was considered as autofluorescence.

## 4. Discussion

In the following section, the data obtained during conducting histological experiments and fluorescence tomography data analysis is discussed in two separate parts and compared to recent literature findings. Also, future outlooks for the way of how to conduct further experiments are given.

### 4.1. Histology

In the following, IHC staining of CD90 and firefly luciferase in Thy-1.2-Luc transgenic and wildtype mice, as well as hematoxylin and eosin staining, will be discussed. Especially for the last one, suggestions for possible improvements and better ways forward are explained in detail.

#### 4.1.1. IHC detection of CD90

One main goal of this thesis was to detect CD90 expression by IHC in tissues and tumors of mice bearing subcutaneously implanted B16F10 melanoma. To obtain reliable and reproducible staining results, three Thy-1.2-Luc transgenic mice injected with  $10^6$  B16F10 melanoma cells and three wildtype mice of the strain C57BL/6 without being injected with melanoma cells were used. To gain ideal results by IHC staining, an additional focus was set on the optimization of a CD90 staining protocol including finding the ideal antibody dilutions and incubation times. Previous optimization has already been done by Lina Pan, but the protocol of anti-CD90 antibody staining was finalized in this thesis. The used polyclonal rabbit anti-CD90 antibody was most effective in a 1:600 dilution. Specific and intense brownish coloration was achieved after DAB reaction indicating successful staining. As staining was similar for each mouse, it can be said that the chosen IHC protocol is reproducible.

Previous experiments of this working group have already shown success in detecting luciferase *in vivo*, which directly correlates to CD90 expression when expressed under the control of the Thy1.2 expression cassette, via BLI (single organ) and DLIT (3D) analysis. Since both *in vivo* analysis methods exhibit similar features to the IHC staining results, one can conclude that staining worked as intended and the results were reliable. Therefore, *in vivo* methods can be successfully combined to *ex vivo* experiments. At this point, it is important to add, that CD90 can be expressed in various tissues, besides brain and skin also in tumors. BLI and DLIT signal, however, can only be detected in murine tissue expressing luciferase under the control of the Thy-1.2 cassette. Due to implantation, the B16F10 melanoma does not express luciferase and therefore no relevant signal can be detected there. However, our results, which show that CD90 is overexpressed in murine as well as transplanted tumors, can be confirmed by literature. To mention just one example, Sauzay *et al.* (2019) stated that the highest CD90

expression can be found in tumor cells directly at the cancer site and also in migrating tumor cells. In this study, the protein is expressed in many tumor types like brain, pancreatic and kidney tumors [68]. According to IHC staining, CD90 is expressed at a similar level both in the wildtype and Thy1.2-Luc transgenic mice. This is due to the fact that they are both from the same inbred strain (C57BL/6 albino). Besides in tumors, CD90 can be detected in high amounts in the brain. Already in the year 1976, Barclay *et al.* described the expression of CD90 in neural cells [27]. Few years later, in 2000, the working group of Feng *et al.* found out that CD90 is specifically activated and expressed in the brain [28]. In between, in 1996, Caroni developed a Thy-1.2 expression cassette, on which a major part of this thesis is based on, taking advantage of the CD90 activation in the brain. With this gene cassette, the CD90-correlating expression of fluorescence proteins or luciferase became possible. [26]. Our results are in agreement with these literature findings because neurons are clearly and intensively stained, indicating high CD90 expression. Furthermore, positive staining can be detected in parts of the skin. According to previous literature, it is known that endothelial cells and lymphatic vessels are overexpressing CD90 [11]. Also, Josvay *et al.* reported CD90 expression in metastases and endothelial cells involved in wound healing and inflammation. This research was based on YFP expression under the control of a Thy-1.2 expression cassette, which was similar to the one used in this experiment [23]. The positively stained parts of the skin in our experiment are proposed to be glands, hair follicles and blood vessels, which are all lined with endothelial cells near the primary tumor and metastases. Since these are tumor associated, CD90 is also overexpressed here, which suits perfectly to the recent literature findings mentioned.

In further experimental steps, controls were performed with an isotype, secondary antibody only and with buffer only to confirm effective positive staining. All control samples were constantly negatively stained, as it was expected. Nevertheless, some of these negatively stained samples showed some brown pigmentation, which is just naturally occurring melanin and should not be associated to a DAB reaction. Negative staining of the control samples provided information about appropriate performance of all stainings, since neither brown background signal nor unspecific staining occurred. As expected, only the dark blue staining of hematoxylin should be and was visible. Although anti-CD90 staining offered good results, the staining method can still be improved by reducing brownish background signal of positively stained samples and by enhancing intensity of blue hematoxylin staining. These improvements could be achieved by optimizing incubation times and the number of washing steps.

#### **4.1.2. IHC detection of firefly luciferase**

Another goal of this thesis was to detect positive luciferase expression in tissues of transgenic Thy1.2-luc mice, to optimize the corresponding staining protocol and to correlate luciferase expression with CD90 protein expression. The original staining protocol from the manufacturer was adapted with the aid of literature and experience. For example, experience showed that staining worked best when using a Tris-EDTA buffer with 0.05% Tween20 for antigen retrieval, because the used antibody required a high pH value. According to the manufacturer, the used antibody worked best in a 1:1000 dilution, which could also be confirmed by the conducted experiment. Only one tested mouse showed some parts in the lung with positive luciferase staining. The positively tested mouse was of the type #1\_4T[PE]Luc, which is used as mouse model for breast cancer. This mouse (BALB/c background) received 4T1 murine triple negative breast cancer cells stably transduced with a lentivirus encoding for firefly luciferase. Luciferase was expressed under the control of the phosphoglycerol (PKG) promoter [67]. Metastasis was observed to be restricted to regional lymph nodes and the lungs, therefore luciferase activity could be observed in IHC staining in parts of the lungs of these mice [69].

As negative control, a mouse (BALB/c background) expressing the NIR fluorescent protein iRFP720 was taken [67]. Since this mouse is luciferase negative, these controls showed almost no brownish coloration, which would be the result of an effective reaction with DAB. In the ideal case, negative controls should not show any signs of DAB reaction. However, in this experiment this unspecific staining and high background signal occurred due to limited resources of blocking serum (normal horse serum), which was responsible for blocking endogenous nucleases. In future, this next step of optimizing luciferase detection will be repeated by another diploma student. It is envisaged to repeat the whole staining protocol suggested by the manufacturer with mice known to have luciferase activity and control animals with the newly ordered and up-to date staining kit.

#### **4.1.3. Hematoxylin and eosin staining**

To perform appropriate determination of cellular structures of the tissues stained, hematoxylin and eosin staining was done as comparison to IHC staining. However, color intensity of hematoxylin staining was too weak when compared to stainings seen in literature. Therefore, the incubation time in hematoxylin and also the subsequent washing times were adapted to gain better results. Due to the fact that these steps did not meet all the expectations, new hematoxylin solution was ordered, since the old one had already been expired at the time of the experiment. Although the new hematoxylin solution could not be tested yet, satisfying results are expected.

## **4.2. Fluorescence tomography data analysis**

The biodistribution of naked siRNA, auropolyplexes loaded with siRNA, cadmium telluride quantum dots and polyethyleneimine-based quantoplexes was tracked to measure ROIs specifically drawn for every organ. The biodistribution of each compound tested is briefly explained, discussed and compared to literature, if already available at the time of writing this thesis.

### **4.2.1. Influence of changing threshold values on FLIT measurements**

The first step of data analysis was to examine the effects of the threshold value on the measurements. To do so, the images with default threshold values were compared to images with decreased and adjusted threshold values. ROIs were drawn identical for both image types and measured the same way. The resulting values were then summarized in one graph for comparison. Both the values at 0 h and 24 h exhibit the same values with and without adjusted threshold, proving that threshold values have no influence on the measurement of ROIs. Therefore, threshold can only be used to adjust and reduce background signal. For further visualization, it was determined to take those images with decreased threshold values due to reduced background signal. Without high background signal, which was visible as blue cloudy structures, relevant signal could be determined easier. In addition to the threshold, also the color scale was adjusted for better visualization. The logarithmic scale made it easier to distinguish between the background signal and the relevant signal because of increased color intensity and brightness.

### **4.2.2. Biodistribution of siRNA-AF750 and QD based nucleic acid formulations**

Firstly, the biodistribution of naked siRNA labelled with AF750 was observed in mice 0 h and 24 h after intravenous injection. To improve CT results, iopamidol was injected intraperitoneally as contrast agent. Immediately after injection, *in vivo* 3D FLIT imaging of the whole body showed that the major AF750 content accumulated in the bladder and to smaller amounts also in the kidney. After 24 h, most signal got excreted by the bladder. At this point, kidney signal decreased by half, compared to the initial signal. 3D FLIT data matched with data of *ex vivo* 2D organ imaging, since only kidneys showed any signal 24 h after injection. These results were similar to those found out by Geyer *et al.*, 2017, who came to the conclusion that the obtained data is an indication of renal excretion [45]. Although this analysis was done as absolute quantification, no exact numbers for excretion can be given because signal could vary

significantly due to the filling level of the bladder. If it is empty, signal intensity decreased and possibly sticks in the cage.

After studying the biodistribution of naked siRNA, the same was done for siRNA-AF750 incorporated into auropolyplexes. This study led to the observation that siRNA-AF750 initially accumulated in the lung and were excreted to some extents by the bladder within 24 h. As data analysis of all three mice showed, biodistribution is similar in every mouse. The reason for the observed initial lung accumulation is due to the way of administration, which was done intratracheally as it was also described by Thanki *et al.*, (2019) [70]. 24 h after administration, signal of siRNA-AF750 was mainly detected in the bladder and the kidneys, but to a higher extent in the bladder. As reviewed by Du *et al.*, 2018, kidneys are responsible for blood filtration and subsequent waste elimination and the bladder mediates excretion of substances. Therefore, these two organs have the task of clearance and elimination of nanoparticles *in vivo*, which, however, strongly depends on the shape, size and surface chemistry of the nanoparticles. Clearance efficiency is higher, the smaller the nanoparticle is. Since the used auropolyplexes are relatively big with approximately 50 nm, clearance works less efficiently [71]. When summing up the amount of siRNA-AF750 at each timepoint (0 h, 24 h) in pmol, it was found out that the average amount of siRNA-AF750 in pmol decreased slightly, which could be the amount of siRNA-AF750 excreted in the experimental period of time or the decay of auropolyplexes. If auropolyplexes decay during the experiment, siRNA-AF750 signal would accumulate in the bladder and the kidneys, as it is the case here, and gold nanoparticles would stay in the lung. However, our results are satisfying because most auropolyplexes stayed in the body for at least one day without having any major side effects.

Genetic material like siRNA can be also incorporated into so called quantoplexes, where the negatively charged siRNA together with quantum dots (bearing a net negative charge) are combined with polycations [58]. In the next biodistribution analysis, first NIR-emitting CdTe quantum dots alone, which were injected intravenously into mice of the strain BALB/c, were indicative of accumulation in the lungs and the liver after 24 h. Two out of three samples also showed weak signals in the kidneys. Although ROIs were drawn very carefully according to the visible kidney contrast of 2D CT images, the detected kidney signals could still be a part of the liver or other organs. To validate these results obtained via FLIT analysis, organ images, which were taken via *ex vivo* epifluorescence FLI, were analyzed. Since no control organs were available for this project, the threshold to reduce background signal was calculated with the aid of organ images including data from treated and control animals from another quantum dot experiment. The organ images collected by Aileen Prosche and Mag. Fatih Alioglu were used to calculate the average threshold value. This value was then applied to the organ images

of this project. Unfortunately, this also induced high variance yielding less accurate results. Although weak kidney signals could be detected in these organ images, this could also be attributed to background signal. However, since this 2D organ data matched with 3D FLIT data, and weak kidney signal was detected in both, the probability of signals detected in the kidneys is increased. In 2007, Choi *et al.* already reported that quantum dots with a hydrodynamic diameter of 5-6 nm are more likely to be excreted rapidly by renal or urinary excretion. Since the NIR-emitting quantum dots used in this experiment fall within this range, renal clearance and resulting signal in the kidneys is entirely possible. Since excretion by the kidneys occurs faster, visibility decreases with time, while nanoparticles are retained for a longer time in the liver resulting in increased toxicity [50]. After extensive literature research, it was assumed that our working group was the first one doing research on the biodistribution of quantum dots via *in vivo* FLIT analysis, therefore, there was no data available for direct comparison at the moment of research.

To continue the quantum dot experiment, quantoplexes, which were loaded with NIR-emitting CdTe quantum dots, PEI and plasmid DNA, were also tested for their biodistribution. Quantoplexes were injected intravenously into mice of the strain BALB/c. The Signal, which were analyzed via 3D FLIT, accumulated mainly in liver and lungs. Other organs like kidneys or bladder showed less intense signals. To validate these results, organ images obtained from *ex vivo* 2D epifluorescence FLI were analyzed. Unfortunately, no control images were available for this project. Therefore, the average threshold signal was calculated with the aid of organ images including data from both treated and control animals from the quantoplex experiment of Patricia Gabler and Mag. Fatih Alioglu. This value was then applied to the organ images of this project, as it was done in the quantum dot experiment already shown. Organ images showed clear signals in liver and lungs. The stomach also showed high signal intensity, but this was thought to be due to autofluorescence because the images were taken filter paired. The findings of the quantoplex experiment shown in this thesis match with those found by Patricia Gabler and Zintchenko *et al.*, 2009, who found that quantoplexes accumulate in liver, lungs and spleen shortly after injection and could be detected in the murine body for at least one week [58].

### **4.3. Conclusion**

To sum up the histological part of this thesis, it can be said, that IHC staining with the anti-CD90 and anti-firefly luciferase antibodies worked as expected and suggested by previous literature. After Thy-1.2-Luc transgenic C57BL/6 mice were treated with a transplantable tumor, extensive CD90 expression could be detected in tumors, brain, endothelial cells and lymphatic vessels in the skin. As expected, both the CD90 expression in transgenic and wildtype

mice was similar. The expression of firefly luciferase in a 4T1 triple negative breast cancer mouse model was detected in parts of the lung under control of the PGK promoter. Due to the IHC's successful staining and significant controls, the protocols used are reproducible. To conclude the second part of this thesis, the biodistribution of naked siRNA, auropolyplexes loaded with siRNA, cadmium telluride quantum dots and polyethyleneimine-based quantoplexes was tracked. 3D images of living mice were taken at two different time-points after manually drawing ROIs. After finding out that adjusting the background thresholds had no effect on measurements, the biodistribution of naked siRNA labeled with AF750 was observed, coming to the conclusion that siRNA mainly accumulated in the kidneys. The same composition incorporated in auropolyplexes resulted in signals in the bladder and kidneys. In case of quantum dots, however, signal was mainly detected in the lungs and the liver, but also weakly in the kidneys. Further quantum dot incorporation into quantoplexes resulted into signal accumulated in liver and lungs. All these findings are agreement with literature, if already available.



## References

- [1] A. L. Mescher, *Junqueira's Basic Histology*, 13th ed. Bloomington, Indiana: McGraw-Hill Education, 2013.
- [2] A. Teti, "Regulation of cellular functions by extracellular matrix," *J. Am. Soc. Nephrol.*, vol. 2, no. 10 SUPPL., 1992.
- [3] A. H. Fischer, K. A. Jacobson, J. Rose, and R. Zeller, "Hematoxylin and eosin staining of tissue and cell sections," *Cold Spring Harb. Protoc.*, vol. 3, no. 5, pp. 4986–4988, 2008.
- [4] Abcam, "What are polyclonal, monoclonal and recombinant antibodies?" [Online]. Available: [abcam.com](http://abcam.com). [Accessed: 21-Oct-2019].
- [5] Abcam, "Direct vs indirect detection in IHC." [Online]. Available: [abcam.com](http://abcam.com). [Accessed: 22-Oct-2019].
- [6] Bioss, "Fluorescent vs. chromogenic detection in immunohistochemistry." [Online]. Available: [blog.biossusa.com](http://blog.biossusa.com). [Accessed: 27-Nov-2019].
- [7] M. Nurjayadi *et al.*, "Immunogenicity and Specificity of Anti recombinant Protein Fim-C-Salmonella typhimurium Antibody as a Model to Develop Typhoid Vaccine," *Procedia Chem.*, vol. 18, no. Mcls 2015, pp. 237–245, 2016.
- [8] Abcam, "DAB staining." .
- [9] Abcam, "Chromogenic detection in IHC." [Online]. Available: [abcam.com](http://abcam.com). [Accessed: 22-Oct-2019].
- [10] G. L. Bratthauer, "The avidin-biotin complex A(BC) method and other avidin-biotin binding methods," *Methods Mol. Biol.*, vol. 588, no. 9, pp. 63–66, 2009.
- [11] K. Schubert, D. Gutknecht, M. Köberle, U. Anderegg, and A. Saalbach, "Melanoma cells use thy-1 (CD90) on endothelial cells for metastasis formation," *Am. J. Pathol.*, vol. 182, no. 1, pp. 266–276, 2013.
- [12] K. A. Zimmermann, "Immune system: diseases, disorders & function." [Online]. Available: [livescience.com](http://livescience.com). [Accessed: 23-Oct-2019].
- [13] G. Jurisic, M. Iolyeva, S. T. Proulx, C. Halin, and M. Detmar, "Thymus cell antigen 1 (Thy1, CD90) is expressed by lymphatic vessels and mediated cell adhesion to lymphatic endothelium," *Exp Cell Res.*, no. 316(17), pp. 2982–2992, 2010.
- [14] T. Kobayashi, Y. Hamaguchi, M. Hasegawa, M. Fujimoto, K. Takehara, and T. Matsushita, "B cells promote tumor immunity against B16F10 melanoma," *Am. J. Pathol.*, vol. 184, no. 11, pp. 3120–3129, 2014.
- [15] S. Shah *et al.*, "Increased rejection of primary tumors in mice lacking B cells: Inhibition of anti-tumor CTL and TH1 cytokine responses by B cells," *Int. J. Cancer*, vol. 117, no. 4, pp. 574–586, 2005.
- [16] D. J. DiLillo, K. Yanaba, and T. F. Tedder, " B Cells Are Required for Optimal CD4 +

- and CD8 + T Cell Tumor Immunity: Therapeutic B Cell Depletion Enhances B16 Melanoma Growth in Mice ,” *J. Immunol.*, vol. 184, no. 7, pp. 4006–4016, 2010.
- [17] I. J. Fidler and G. L. Nicolson, “Organ selectivity for implantation survival and growth of b16 melanoma variant tumor lines,” *J. Natl. Cancer Inst.*, vol. 57, no. 5, pp. 1199–1202, 1976.
- [18] C. Danciu *et al.*, “Behaviour of four different B16 murine melanoma cell sublines: C57BL/6J skin,” *Int. J. Exp. Pathol.*, vol. 96, no. 2, pp. 73–80, 2015.
- [19] A. Kumar, A. Bhanja, J. Bhattacharyya, and B. G. Jaganathan, “Multiple roles of CD90 in cancer,” *Tumor Biol.*, vol. 37, no. 9, pp. 11611–11622, 2016.
- [20] R. Herrera-Molina *et al.*, *Thy-1-interacting molecules and cellular signaling in Cis and Trans*, vol. 305. 2013.
- [21] S. M. M. Haeryfar and D. W. Hoskin, “Thy-1: More than a Mouse Pan-T Cell Marker,” *J. Immunol.*, vol. 173, no. 6, pp. 3581–3588, 2004.
- [22] A. E. Reif, “Immune cytotoxicity of mouse thymic lymphocytes,” *J. Immunol.*, p. 91:557, 1963.
- [23] K. Józsvay *et al.*, “Besides neuro-imaging, the Thy1-YFP mouse could serve for visualizing experimental tumours, inflammation and wound-healing,” *Sci. Rep.*, vol. 4, pp. 1–7, 2014.
- [24] H. Reeh *et al.*, “Response to IL-6 trans- A nd IL-6 classic signalling is determined by the ratio of the IL-6 receptor  $\alpha$  to gp130 expression: Fusing experimental insights and dynamic modelling,” *Cell Commun. Signal.*, vol. 17, no. 1, pp. 1–21, 2019.
- [25] T. H. Barker and J. S. Hagood, “Getting a grip on Thy-1 signaling,” *Biochim. Biophys. Acta - Mol. Cell Res.*, vol. 1793, no. 5, pp. 921–923, 2009.
- [26] P. Caroni, “Overexpression of growth-associated proteins in the neurons of adult transgenic mice,” *J. Neurosci. Methods*, vol. 71, no. 1, pp. 3–9, 1997.
- [27] A. Neil Barclay, M. Letarte-Muirhead, A. F. Williams, and R. A. Faulkes, “Chemical characterisation of the Thy-1 glycoproteins from the membranes of rat thymocytes and brain,” *Nature*, vol. 263, no. 5578, pp. 563–567, 1976.
- [28] G. Feng *et al.*, “Imaging Neuronal Subsets Neurotechnique,” *Neuron*, vol. 28, pp. 41–51, 2000.
- [29] R. Paulmurugan and S. S. Gambhir, “Firefly luciferase enzyme fragment complementation for imaging in cells and living animals,” *Anal Chem.*, no. 77(5), pp. 1295–1302, 2005.
- [30] T. V. Brennan, L. Lin, X. Huang, and Y. Yang, “Generation of luciferase-expressing tumor cell lines,” *Bio protoc.*, no. 8(8), pp. 1–16, 2018.
- [31] Merck, “Bioluminescent firefly luciferase assays.” [Online]. Available: [sigmaaldrich.com](http://sigmaaldrich.com). [Accessed: 18-Mar-2020].

- [32] C. H. Johnson, T. S. Fisher, L. T. Hoang, B. H. Felding, G. Siuzdak, and P. J. O'Brien, "Luciferase does not alter metabolism in cancer cells," *Metabolomics*, vol. 10, no. 3, pp. 354–360, 2014.
- [33] E. Conti, N. P. Franks, and P. Brick, "1 LCI - firefly luciferase." [Online]. Available: rcsb.org. [Accessed: 18-Mar-2020].
- [34] K. V. Wood, "The bioluminescence advantage," *Promega Corporation online*, 2007. .
- [35] J. K. Tung, K. Berglund, C.-A. Gutekunst, U. Hochgeschwender, and R. E. Gross, "Bioluminescence imaging in live cells and animals," *Neurophotonics*, vol. 3, no. 2, p. 025001, 2016.
- [36] F. Alioglu, J. Scholda, K. Singeorzan, A. Prosche, M. Ogris, and H. Sami, "Combined Fluorescence molecular tomography and computed tomography ( FMT / CT ) to track and quantify systemically applied NIR-dye labeled nucleic acid," pp. 1–16.
- [37] G. Süel, "Use of Fluorescence Microscopy to Analyze Genetic Circuit Dynamics," vol. 497, pp. 275–293, 2011.
- [38] O. Shimomura, F. H. Johnson, and Y. Saiga, "Extraction, purification and properties of aequorin, a bioluminescent protein from the luminous hydromedusan, aequorea," *J. Cell. Comp. Physiol.*, vol. 59, no. 165, pp. 223–239, 1962.
- [39] R. M. Hoffman, *Live cell imaging in live animals with fluorescent proteins*, 1st ed., vol. 506. Elsevier Inc., 2012.
- [40] R. Y. Tsien, "The Green Fluorescent Protein," *Annu. Rev. Biochem.*, vol. 67, no. 1, pp. 509–544, 1998.
- [41] R. Y. Tsien, "Constructing and exploiting the fluorescent protein paintbox (Nobel Lecture).," *Angew. Chem. Int. Ed. Engl.*, vol. 48, no. 31, pp. 5612–5626, 2009.
- [42] M. V. Matz *et al.*, "Fluorescent proteins from nonbioluminescent Anthozoa species," *Nat. Biotechnol.*, vol. 17, no. 10, pp. 969–973, 1999.
- [43] L. Rowe, E. Dikici, and S. Daunert, "Engineering bioluminescent proteins: expanding their analytical potential," *Anal Chem*, vol. 81, no. 21, pp. 1–14, 2009.
- [44] Abcam, "Understanding fluorophores," 2020. [Online]. Available: abcam.com. [Accessed: 05-May-2020].
- [45] A. Geyer *et al.*, "Fluorescence- and computed tomography for assessing the biodistribution of siRNA after intratracheal application in mice," *Int. J. Pharm.*, vol. 525, no. 2, pp. 359–366, 2017.
- [46] Bioquest, "Spectra," 2019. .
- [47] J. L. Ballard, V. K. Peeva, C. J. S. DeSilva, J. L. Lynch, and N. R. Swanson, "Comparison of Alexa Fluor® and CyDye™ for practical DNA microarray use," *Mol. Biotechnol.*, vol. 36, no. 3, pp. 175–183, 2007.
- [48] U. Resch-Genger, M. Grabolle, S. Cavaliere-Jaricot, R. Nitschke, and T. Nann,

- “Quantum dots versus organic dyes as fluorescent labels,” *Nat. Methods*, vol. 5, no. 9, pp. 763–775, 2008.
- [49] A. L. Rogach and M. Ogris, “Near-infrared-emitting semiconductor quantum dots for tumor imaging and targeting,” *Curr. Opin. Mol. Ther.*, vol. 12, no. 3, p. 9, 2010.
- [50] H. Soo Choi *et al.*, “Renal clearance of quantum dots,” *Nat. Biotechnol.*, vol. 25, no. 10, pp. 1165–1170, 2007.
- [51] F. Stuker, J. Ripoll, and M. Rudin, “Fluorescence molecular tomography: Principles and potential for pharmaceutical research,” *Pharmaceutics*, vol. 3, no. 2, pp. 229–274, 2011.
- [52] A. Cantatore and P. Müller, “Introduction to computed tomography,” *DTU Mech. Eng.*, pp. 1–77, 2011.
- [53] J.-C. Tseng and K. D. Vasquez Jeffrey Peterson, “Optical imaging on the IVIS spectrumCT system: general and technical considerations for 2D and 3D imaging,” *PerkinElmer*, no. 1, pp. 1–18, 2015.
- [54] H. Dana *et al.*, “Molecular Mechanisms and Biological Functions of siRNA.,” *Int. J. Biomed. Sci.*, vol. 13, no. 2, pp. 48–57, 2017.
- [55] W. H. De Jong and P. J. A. Borm, “Drug delivery and nanoparticles: Applications and hazards,” *Int. J. Nanomedicine*, vol. 3, no. 2, pp. 133–149, 2008.
- [56] A. Taschauer *et al.*, “Combined chemisorption and complexation generates siRNA nanocarriers with biophysics optimized for efficient gene- knockdown and air-blood barrier crossing Combined chemisorption and complexation generates siRNA nanocarriers with biophysics optimized for,” *ACS Appl. Mater. Interfaces*.
- [57] W. G. Kreyling *et al.*, “Air-blood-barrier translocation of tracheally instilled gold nanoparticles inversely depends on particle size,” *ACS Nano*, vol. 8, no. 1, pp. 222–233, 2014.
- [58] A. Zintchenko *et al.*, “Drug Nanocarriers Labeled With Near-infrared- emitting Quantum Dots ( Quantoplexes ): Imaging Fast Dynamics of Distribution in Living Animals,” *Mol. Ther.*, vol. 17, no. 11, pp. 1849–1856, 2009.
- [59] Y.-C. Yeh, “Gold Nanoparticles: Perparation, Properties, and Applications in Bionanotechnology,” vol. 4, no. 6, pp. 1871–1880, 2012.
- [60] N. Limjunyawong, J. Mock, and W. Mitzner, “Instillation and fixation methods useful in mouse lung cancer research,” *J. Vis. Exp.*, vol. 2015, no. 102, pp. 1–9, 2015.
- [61] Abcam, “IHC staining protocol for paraffin, frozen and free floating sections,” 2020. .
- [62] J. Myers, “Overview of heat-induced epitope retrieval (HIER) techniques and devices,” 2011. .
- [63] G. L. Bratthauer, “CHAPTER 20 The Peroxidase-Antiperoxidase Method \* ( PAP ),” vol. 34, pp. 165–173, 1994.
- [64] Bio-rad, “Incubate with secondary antibody and/or amplification reagent,” 2020.

- [Online]. Available: bio-rad-antibodies.com. [Accessed: 06-May-2020].
- [65] IHCworld, "Blocking endogenous peroxidase," 2011. .
- [66] N. Alwahaibi, S. Aljaradi, and H. Alazri, "Alternative to xalene as a clearing agent in histopathology," *J. Lab. Physicians*, vol. 10, no. 2, pp. 189–193, 2018.
- [67] A. Geyer *et al.*, "Multimodal Fluorescence and Bioluminescence Imaging Reveals Transfection Potential of Intratracheally Administered Polyplexes for Breast Cancer Lung Metastases," *Hum. Gene Ther.*, vol. 28, no. 12, pp. 1202–1213, 2017.
- [68] C. Sauzay, K. Voutetakis, A. A. Chatziioannou, E. Chevet, and T. Avril, "CD90/Thy-1, a cancer-associated cell surface signaling molecule," *Front. Cell Dev. Biol.*, vol. 7, no. APR, pp. 1–11, 2019.
- [69] V. P. Baklaushev *et al.*, "Luciferase expression allows bioluminescence imaging but imposes limitations on the orthotopic mouse (4T1) model of breast cancer," *Sci. Rep.*, vol. 7, no. 1, pp. 1–17, 2017.
- [70] K. Thanki *et al.*, "Mechanistic profiling of the release kinetics of siRNA from lipidoid-polymer hybrid nanoparticles in vitro and in vivo after pulmonary administration," *J. Control. Release*, vol. 310, no. August, pp. 82–93, 2019.
- [71] B. Du, M. Yu, and J. Zheng, "Transport and interactions of nanoparticles in the kidneys," *Nat. Rev. Mater.*, vol. 3, no. 10, pp. 358–374, 2018.

## List of figures

Figure 1: Direct versus indirect detection method in immunohistochemistry .....	10
Figure 2: Oxidation of DAB into brownish precipitate.....	11
Figure 3: Schematic diagram of the avidin-biotin complex (ABC) procedure.....	12
Figure 4: Thy-1 (CD90) signaling .....	15
Figure 5: Thy-1.2 expression cassette .....	16
Figure 6: Protein structure and oxidation of D-luciferin to oxyluciferin .....	17
Figure 7: Emission spectra of Alexa fluor and cyanine dyes in the near infrared .....	19
Figure 8: Principle of fluorescence imaging tomography (FLIT) .....	22
Figure 9: Calibration curve for calculation of AF750 amount .....	34
Figure 10: Workflow and timeline of siRNA-AF750 experiment .....	35
Figure 11: Workflow and timeline of auropolyplex experiment.....	36
Figure 12: Workflow and timeline of quantum dot experiment .....	36
Figure 13: Workflow and timeline of quantoplex experiment .....	37
Figure 14: Hematoxylin and eosin staining of brain, tumor and skin of MCT-180.....	39
Figure 15: IHC staining of brain, tumor and skin of Thy-1.2-Luc transgenic mouse MCT-172 .....	40
Figure 16: IHC staining of brain, tumor and skin of Thy-1.2-Luc transgenic mouse MCT-173 .....	41
Figure 17: IHC staining of brain, tumor and skin of Thy-1.2-Luc transgenic mouse MCT-179 .....	42
Figure 18: IHC staining of brain, tumor and skin of wild type mouse MCT-356 .....	43
Figure 19: IHC staining of brain, tumor and skin of wildtype mouse MCT-357 .....	44
Figure 20: IHC staining of brain, tumor and skin of wildtype mouse MCT-358 .....	45
Figure 21: Detection of luciferase in the lung via IHC .....	46
Figure 22: Effect of default and adjusted threshold values on ROI measurement for 3D FLIT analysis .....	48
Figure 23. 3D signal reconstruction and 2D epifluorescence FLI organ imaging of naked siRNA-AF750 .....	49
Figure 24: 3D FLIT signal distribution of naked siRNA-AF750 after 0 h and 24 h .....	51
Figure 25: 3D FLIT signal distribution of auropolyplexes loaded with siRNA-AF750 after 0 h and 24 h .....	53
Figure 26: 3D FLIT signal distribution of quantum dots 0 h and 24 h after injection .....	55
Figure 27: Ex vivo epifluorescence FLI organ images of quantum dots experiments .....	56
Figure 28: 3D FLIT signal distribution of quantoplexes 0 h and 24 h after injection .....	58
Figure 29: Ex vivo epifluorescence FLI organ images of quantoplex experiment.....	60

## List of tables

Table 1: List of used reagents including their supplier and catalog nr .....	24
Table 2: List of used machines including their supplier .....	26
Table 3: List of used materials including their supplier .....	26
Table 4: List of used software including their supplier .....	27
Table 5: Information to all mice used in IHC .....	33

## List of abbreviations

ABC	Avidin-biotin complex
AF750	Alexa Fluor 750
ATP	Adenosine triphosphate
BLI	Bioluminescence imaging
bp	Basepair
BSA	Bovine serum albumin
CdTe	Cadmium telluride
CT	Computed tomography
DAB	3,3'-diaminobenzidine tetrahydrochloride
DLIT	Diffuse luminescence imaging tomography
DNA	Deoxyribonucleic acid
ECM	Extracellular matrix
EDTA	Ethylenediaminetetraacetic acid
EtOH	Ethanol
FDA	Food and Drug Administration
FITC	Fluorescein-5-isothiocyanate
FLI	Fluorescence imaging
FLIT	Fluorescence imaging tomography
FMT	Fluorescence mediated tomography
FRET	Fluorescence resonance energy transfer
GFP	Green fluorescence protein
GPI	Glycosylphosphatidylinositol
H&E	Hematoxylin and eosin staining
HBS	HEPES buffered saline
HDMEC	Human dermal microvascular endothelial cells
HIER	Heat induced antigen retrieval
i. t.	Intratracheal
i. v.	Intravenous
ICP-MS	Inductively coupled plasma mass spectrometry
IgG	Immunoglobulin G
IHC	Immunohistochemistry
LPEI	Linear polyethylenimine
LSAB	Labeled streptavidin-biotin binding
MIP	Maximum intensity projection
MRI	Magnetic resonance imaging
NIR	Near infrared

PAP	Peroxidase-anti peroxidase
PBS	Phosphate buffered saline
PEI	Polyethylenimine
PET	Position emission tomography
RFP	Red fluorescence protein
RNA	Ribonucleic acid
RNAi	RNA interference
ROI	Region of interest
s. c.	Subcutaneous
siRNA	Small interfering RNA
TCR	T cell receptor
TEM	Transmission electron microscopy
Tris	Tri-sodium citrate dihydrate